TU Delft

Delft University of Technology

Document Version
Final published version

Licence
Dutch Copyright Act (Article 25fa)

Citation (APA)
Chand, A., Ali, N., & Tariq, A. (2026). Experimental investigation of flow and heat transfer characteristics in the bend region of matrix channel. *Experimental Thermal and Fluid Science*, *172*, Article 111632. https://doi.org/10.1016/j.expthermflusci.2025.111632

Important note
To cite this publication, please use the final published version (if applicable).
Please check the document version above.

Copyright
In case the licence states “Dutch Copyright Act (Article 25fa)”, this publication was made available Green Open Access via the TU Delft Institutional Repository pursuant to Dutch Copyright Act (Article 25fa, the Taverne amendment). This provision does not affect copyright ownership.
Unless copyright is transferred by contract or statute, it remains with the copyright holder.

Sharing and reuse
Other than for strictly personal use, it is not permitted to download, forward or distribute the text or part of it, without the consent of the author(s) and/or copyright holder(s), unless the work is under an open content license such as Creative Commons.

Takedown policy
Please contact us and provide details if you believe this document breaches copyrights.
We will remove access to the work immediately and investigate your claim.

This work is downloaded from Delft University of Technology.

Experimental Thermal and Fluid Science 172 (2026) 111632

Contents lists available at ScienceDirect

Experimental Thermal and Fluid Science

journal homepage: www.elsevier.com/locate/etfs

Experimental investigation of flow and heat transfer characteristics in the bend region of matrix channel

Arun Chand [a], Nishab Ali [b], Andallib Tariq [a,*]

[a] AVTAR (Aerodynamics Visualization and Thermal Analysis Research) Lab, Mechanical and Industrial Engineering Department Indian Institute of Technology Roorkee, Roorkee 247667, India
[b] Resources & Recycling, Faculty of Civil Engineering and Geosciences, TU Delft, the Netherlands

ARTICLE INFO

Keywords:
Matrix cooling
Serpentine channel
Dean vortices
Heat transfer
Particle Image Velocimetry
Liquid crystal thermography

ABSTRACT

Matrix cooling is gaining attention as an advanced internal cooling strategy for gas turbines, offering both enhanced mechanical integrity and superior heat transfer. However, the aerothermal behavior in bend regions, especially downstream of the matrix, remains insufficiently explored. This study presents a detailed experimental investigation of flow dynamics and heat transfer across the bend section that occurs downstream of the matrix channel. Two matrix configurations, i.e., (i) 3-subchannel (3SC) and (ii) 4-subchannel (4SC), are systematically studied at Reynolds numbers (*Re*) of 5,000, 7,500, and 10,000. High-resolution particle image velocimetry (PIV) and liquid crystal thermography (LCT) techniques have been used for multi-plane aerothermal measurements to elucidate the correlation of complex flow with thermal fields. Results indicate that the matrix emanates the corotating vortices, leading to spatially non-uniform secondary flows, including the emergence of Dean-type vortices at the downstream bend. In particular, the 4SC matrix promotes stronger vortex-driven mixing, yielding significant local and average heat transfer enhancement in the bend region. At $Re = 10{,}000$, the 4SC channel achieves a peak heat transfer augmentation of 133 % relative to a smooth baseline, while incurring only a slight increase in friction factor. Across all conditions, the 3SC and 4SC configurations deliver thermal performance factors (TPF) of up to 2.09 and 2.34, respectively. These findings support the potential of matrix cooling to deliver high thermal effectiveness in next-generation internal cooling applications.

1. Introduction

Modern gas turbines operate at turbine inlet temperatures of 1700 °C and higher to maximize thermal efficiency and specific power output. Consequently, blade materials are exposed to gas temperatures far exceeding their melting points, necessitating advanced internal cooling techniques to ensure component longevity and reliability [1]. Matrix or latticework cooling has emerged as a promising internal cooling technique for gas turbine airfoils, offering both superior heat transfer augmentation and enhanced structural rigidity [2,3]. With matrix-cooling, turbine blade is integrated with a matrix of intersecting cooling air channels (Fig. 1). The matrix structure consists of co-planar ribs intersecting at any angle (denoted as β). As air enters the duct, it divides to flow within multiple subchannels in the upper and lower halves. Upon reaching the end of any subchannel, i.e., near the side wall, the flow turns an angle of 2β and enters the opposite half (upper/lower side) subchannels. The impingements and flow turning at the side walls result in significant heat transfer enhancement in these local zones [4]. The path of coolant airflow within the matrix sub-channels, along with the actual turbine blade with matrix cooling, as represented by Goreloff et al. [5], is illustrated in Fig. 1.

Previous studies have explored a range of matrix rib geometries and sub-channel configurations. Goreloff et al. [5] were the first to measure the heat transfer in matrix passages with various rib inclination angles ($\beta = 30°$–$120°$) and Reynolds numbers (5000—20000). It was reported that $\beta = 45°$ provided the highest Nusselt number enhancements. Bunker [6] investigated heat transfer coefficients and pressure losses in a rectangular duct with matrix channels with 45° rib inclination. The findings indicate that the heat transfer enhancements range between 2.5 and 3. Saha et al. [7] studied the matrix structure in the trailing region of the blade and observed thermal enhancement factors in the range of 3 to 4. Deng et al. [8] investigated matrix geometries with a gap in sidewalls (open matrix) and observed lower pressure penalties and lower average heat transfer increment. Carcasci et al. [2] examined the effects of rib thickness and subchannel count (4 and 6 subchannels) on thermal

* Corresponding author.
E-mail address: atariq@me.iitr.ac.in (A. Tariq).

https://doi.org/10.1016/j.expthermflusci.2025.111632
Received 6 August 2025; Received in revised form 12 September 2025; Accepted 15 October 2025
Available online 23 October 2025
0894-1777/© 2025 Elsevier Inc. All rights are reserved, including those for text and data mining, AI training, and similar technologies.

Nomenclature

A	cross-sectional area of rectangular channel (mm^2)
D_h	hydraulic diameter of channel (mm)
f	Friction factor in matrix channel
f_0	Friction factor in smooth channel i.e. without matrix
h	heat transfer coefficient (W/m^2K)
h_c	matrix rib height (mm)
H	height of rectangular channel (mm)
k_a, k_w	thermal conductivity of air andperspex (W/mK)
L	Length of matrix structure
$\dot{m}$	mass flow rate (kg/s)
Nu	Nusselt number in matrix channel, ($Nu = hD_h/k_a$)
Nu_0	Nusselt number for smooth channel (without matrix)
Nu/Nu_0	augmentation Nusselt number
Re	Reynold number, ($Re = \dot{m}D_h/\mu A$)
t	thickness of matrix rib (mm)
t_i	thickness of matrix rib at inlet (mm)
T_i	initial temperature of LC (°C)
T_w	wall temperature at time, t (°C)
T_a	bulk air temperature (°C)
u, v, *and* w	velocity in x ,y, and z direction (m/s)
$V_{xy/yz/xz}$	in-plane velocity, $\sqrt{u^2+v^2}$, $\sqrt{v^2+w^2}$, $\sqrt{u^2+w^2}$ (m/s)
w_{avg}	average flow velocity in the z-direction, (m/s)
w_c	width of the matrix sub-channel (mm)
w_i	width of the matrix sub-channel at inlet (mm)
w_0	centerline velocity (m/s)
W	width (mm)

Greek

α_w	thermal diffusivity of perspex (m^2/s)
β	matrix rib angle
δ	uncertainty
λ_2	λ_2- criterion
μ	dynamic viscosity of air (Pa-s)
υ	kinematic viscosity of air (m^2/s)
ω^*	normalized vorticity

Abbreviations

LCT	liquid crystal thermography
PIV	particle image velocimetry
TKE	turbulent kinetic energy (m^2/s^2)
TPF	thermal performance factor

performance with Reynolds numbers from 2000 to 12,000. Heat transfer enhancement factors of ~ 2.5 for $Re < 6000$ and 2.0–2.5 for $Re > 6000$ were reported. Also, rib thickness has a negligible impact on the heat transfer and matrix geometries, with fewer subchannels performing better than those with more subchannels.

Bu et al. [9] perform both experimental and CFD analysis to systematically examine the effect of rib angle, rib-to-subchannel ratio, and rib density on thermal performance of matrix channels. It was reported that the thermal-performance factor peaked between 45° and 55° and at 3–4 subchannels. Additionally, an increasing number of subchannels increases the friction penalty faster than heat transfer. Prajapati and Tariq [10] conducted experimental investigations on matrix cooling channels using liquid crystal thermography, examining the effects of rib angle (35°, 45°, and 55°) and subchannel aspect ratio (0.4, 0.8, and 1.2) on heat transfer and pressure drop characteristics for Reynolds numbers 5800–14000. Their study revealed that for lower Reynolds numbers ($Re \leq 10000$), the 45° rib angle with subchannel aspect ratio of 0.8 (having four subchannels) provided the highest thermal performance, while for $Re \geq 10000$, matrix with 35° rib angle and four subchannels or 45° rib angle and three subchannels showed superior thermal performance.

Recently, Li et al. [11]conducted systematic numerical investigations on conjugate heat transfer in latticework channels across Reynolds numbers 100–1000, demonstrating that longitudinal vortices generated by the matrix structure enhance heat transfer by 3–10 times compared to straight channels. The study revealed that reducing rib width and increasing channel aspect ratio can achieve heat transfer improvements of 28–69% and 38–70% respectively. Ruan et al. [12] demonstrated that U-shaped latticework structures with perforations enhance heat transfer by 21.6–37.0 % through flow mixing and impingement effects while minimizing pressure loss. Li et al. [13] demonstrated that multi-jet

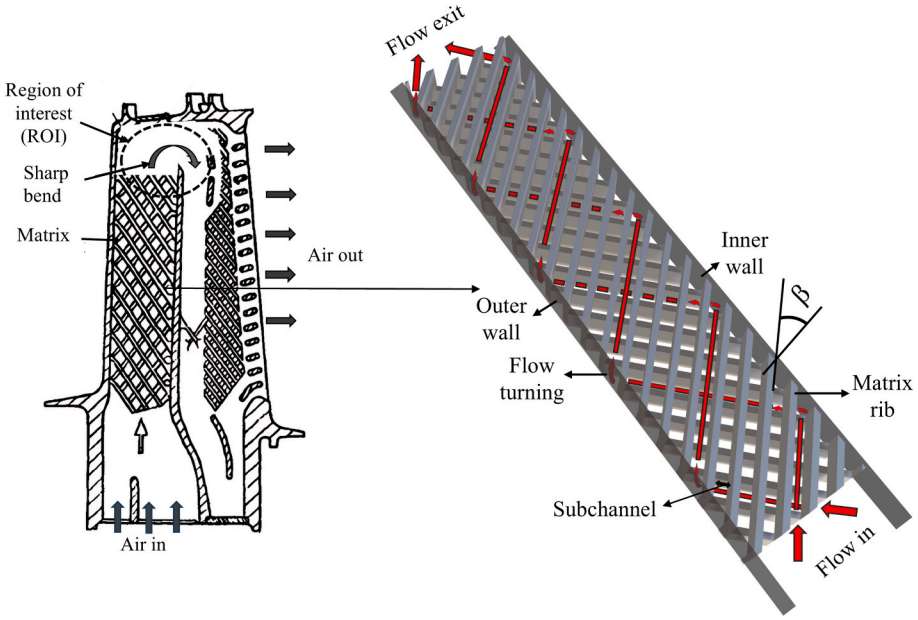

Fig. 1. Actual profile of gas turbine blade with matrix cooling [1] and illustration of fluid flow inside the matrix structure.

impingement in matrix structures significantly improves heat transfer uniformity by generating longitudinal vortices and complex secondary flows. Recent innovations have integrated shape memory alloys (SMA) with traditional latticework geometries renowned for their superior heat transfer characteristics to create next-generation adaptive thermal management systems that automatically transform between straight-channel and latticework configurations based on temperature variations [14]. Wang et al. [15] demonstrated that SMA-enabled latticework structures achieve dual-mode functionality, providing 70% pump power reduction in straight-channel mode while delivering 80 % heat transfer enhancement when activated into latticework configuration through thermally-induced SMA deformation. Li et al. [16] also investigated adaptive latticework design using shape memory alloys (SMA) strips in heat exchanger. The active control of SMA strips regulates the induced vortices and secondary flows in the channel and improves thermal performance.

The above literature has meticulously documented the influence of matrix geometry and flow parameters on the aerothermal characteristics of the matrix cooling channel. However, the scope has been confined within the subchannels or the bottom wall of matrix structure, focusing solely on single straight channels. Contrarily, the actual profile of gas turbine blades incorporating matrix cooling reveals the presence of a 180° sharp bend located downstream of the matrix structure [5]. Recently, Ali and Tariq [17] examined the aerothermal characteristics along a 180° sharp bend in smooth duct, and it was reported that heat transfer increases up to two-fold in the bend region compared to upstream straight section. Another investigation by Ali and Tariq [18] in the bend region of matrix-cooled serpentine channel reported that the vortex flow emanates from the matrix structure, improving the average heat transfer. This study was limited to the vortex development in the first pass of channel for a single turbulent flow condition (Re = 6500) and matrix geometry (3SC matrix). The study lacked a comprehensive analysis to deal with the effect of matrix subchannels and Reynolds number on flow structures and localized heat transfer over the bend regime.

It is crucial to investigate the bend region from an aerothermal perspective, as local hotspots may arise in the region and lead to the premature failure of the blades. Many other engineering applications, such as heat exchangers [19,20], electronic device cooling [21,22], and fuel cells [23] utilize serpentine cooling channels. The aerothermal behavior across bend regions is critical for overall cooling performance in these applications. The sudden change in flow direction at the bend often induces complex vortical structures, resulting in highly non-uniform surface heat transfer with localized enhancement and suppression zones, and pressure drop penalty [24–26]. A detailed understanding of these flow and heat transfer phenomena is essential for optimizing cooling designs and improving system reliability. In particular, matrix-cooled serpentine channels, which introduce turbulence-promoting subchannels upstream of the bend, offer a promising strategy for enhanced thermal performance. However, the flow progression and associated heat transfer mechanisms within the bend, especially in the presence of matrix structures, remain insufficiently explored.

Consequently, in the present effort, a detailed aerothermal characterization across a 180° bend downstream of matrix structures has been carried out. Two matrix configurations, i.e., matrix structure with three subchannels (3SC) and four subchannels (4SC), and rib angle of 45° are considered. These geometric parameters were selected based on previous studies [9,10] demonstrating optimal thermal performance for matrix structure with 45° rib angles and subchannel aspect ratios ranging from 0.8 (4SC) to 1.2 (3SC). The matrix elements are positioned in the first pass at $2D_h$ distance upstream of the bend, focusing specifically on bend-region phenomena rather than the complete serpentine channel configuration, as illustrated in Fig. 1.

Particle image velocimetry (PIV) and transient liquid crystal thermography (TLCT) techniques are employed to capture detailed flow dynamics and thermal characteristics, respectively. Experiments are performed for three turbulent conditions with Reynolds numbers, Re = 5000, 7500, and 10000. This Reynolds number range is also relevant to other applications, including heat exchangers, electronics and electric vehicle battery cooling, where matrix-cooling may provide effective thermal management. Results across the horizontal plane (streamwise flow patterns) and vertical planes (cross-stream flow characteristics) are analyzed to provide comprehensive three-dimensional flow visualization. The investigation examines the evolution of primary/main and secondary flows, vortex interactions, and their correlation with surface heat transfer distribution within the bend. The primary objective is to explain fundamental mechanisms of matrix-induced flow manipulation in serpentine channel configurations. These findings contribute fundamental insights into flow behavior downstream of matrix structures as they traverse sharp bends, which typically occurs in a wide range of engineering applications such as gas turbine blades [24,27], fluid machinery [28–30], and heat exchangers [20]. The comprehensive experimental dataset provides a valuable validation benchmark for computational modeling efforts in this domain.

2. Experimental details

The experimental setup used for fluid flow and heat transfer characterization is illustrated schematically in Fig. 2a, with the actual facility developed at the AVTAR Lab, IIT Roorkee, shown in Fig. 2b. The major components comprise a two-pass serpentine channel, controlled airflow system, particle image velocimetry (PIV) measurement system, and liquid crystal thermography (LCT) system. The serpentine channel here refers to two-pass rectangular duct (Fig. 3a) with a width, W = 150 mm and height, H = 46 mm (H ~ W/3). This gives an aspect ratio, AR (W/H) ≈ 3 and hydraulic diameter, D_h = 70.4 mm (D_h ~ W/2). The 180° turn region of serpentine channel has a divider wall with a thickness of 150 mm (= W), replicating a sharp bend geometry representative of practical cooling channel configurations.

The channel is constructed using high-grade, transparent Perspex sheets having low thermal conductivity and diffusivity. This allows optimal optical access for the camera and laser system during PIV and LCT image acquisition along with low heat penetration for transient heat transfer experiment. Matrix structure is positioned $2D_h$ upstream of the bend entrance, spanning the complete channel cross-section. Two geometric configurations are examined: three-subchannel (3SC) and four-subchannel (4SC) matrix with rectangular shape and 45° rib orientations relative to the sidewalls (Fig. 3b). These configurations were selected based on established thermal performance characteristics documented in pertinent literature mentioned in **section 1**. The detailed geometric specifications of matrix structure are shown in Table 1.

Experiments are performed for turbulent inflow conditions corresponding to three Reynolds numbers (Re = 5000, 7500 and 10000). Reynolds number is calculated as $Re = \dot{m}D_h/\mu A$, where $\dot{m}$, A and μ are the mass flow rate, cross-sectional area, and dynamic viscosity of air at channel inlet, respectively. The mass flow rate is measured using a vortex flow meter (see Fig. 2a) and corresponds to 31 kg/hr, 47 kg/hr and 62 kg/hr for Re = 5000, 7500 and 10000, respectively. Prior to the main experiments, the average velocities obtained from the vortex flow meter were cross verified against PIV measurements.

Flow physics is captured at various cross-stream planes (x–y and y–z), and a streamwise (x–z) plane positioned at channel mid-height ($y/h_c = 1$), as shown in Fig. 4. These selected planes capture the flow structure upstream, at, and downstream of the bend, including key locations such as $P^3_{x\text{-}y}$ (0° plane just before the bend), $P^6_{y\text{-}z}$ (90° turn), and $P^8_{x\text{-}y}$ (180° exit plane). For heat transfer measurement, transient liquid crystal thermography is employed to obtain the temperature distribution across the bottom test surface (across bend section), and heat transfer coefficient (h). Contour plots are appropriately scaled along coordinate axes to enhance visualization.

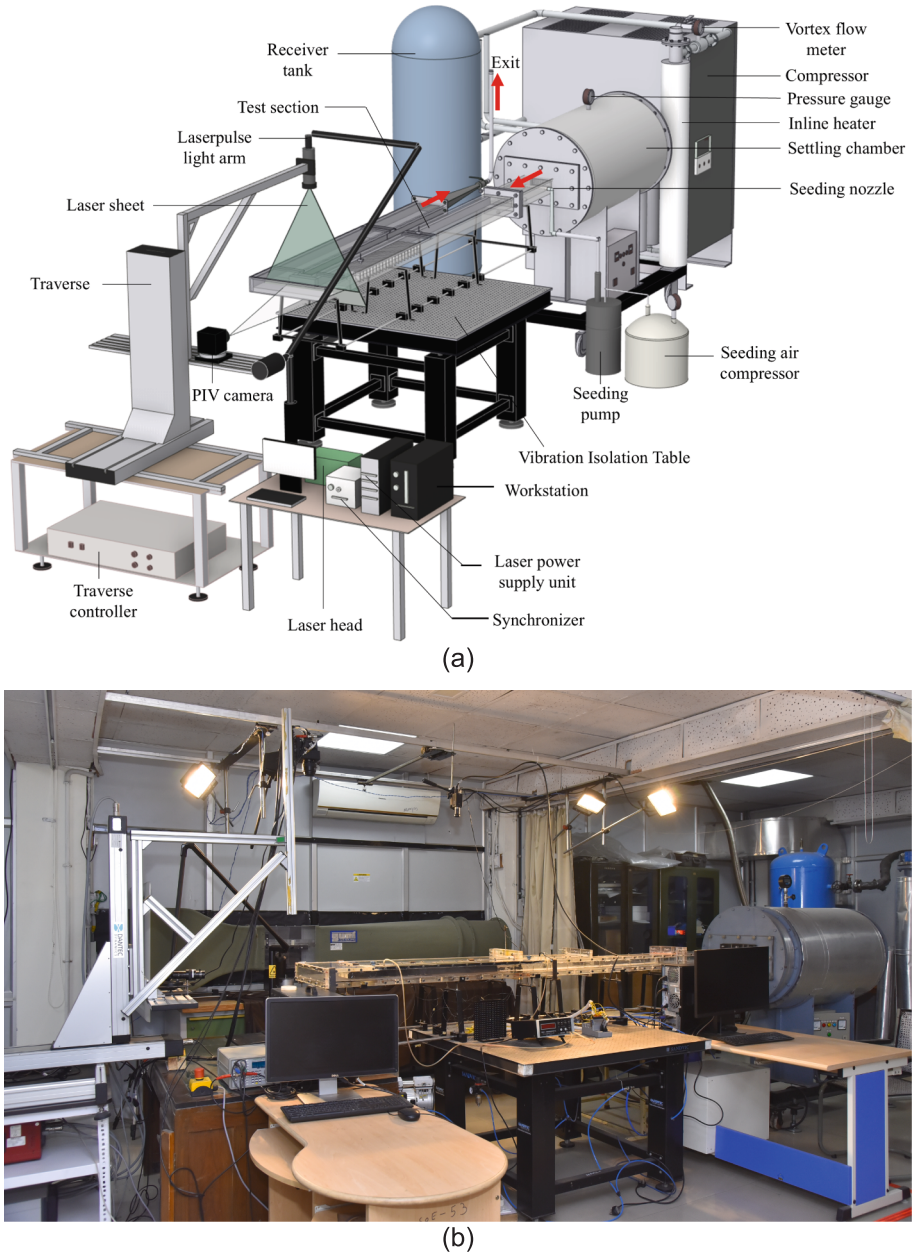

Fig. 2. (a) Schematic of experimental facility with major components and instrumentation, (b) actual view of experimental facility.

2.1. PIV setup and methodology

The system consists of a tracer particle generation arrangement (Laskin, model-9307), a laser emitter, a camera, a traversing mechanism, and a workstation equipped with specialized software (INSIGHT 4G™ TSI) for image capture, processing, and analysis. The concentration of olive oil tracer particle (size ~ 1 μ*m*) generated by the Laskin atomizer is adjusted by controlling the pressure of the compressed air. A double-pulsed Nd: YAG laser system (Quantel, EverGreen 145 mJ @532 nm) produces a laser pulse, which is directed by an optical light arm to the measurement location. The end of the light arm is equipped with special spherical and cylindrical lenses to convert the laser beam into a sheet of thickness approx. ~ 1 mm. A Power-View Plus camera (12 bit, 4MP resolution) coupled with Nikon lens (50 mm focal length) is used to capture the flow images. The laser pulses and camera are synchronized with the help of a TSI synchronizer (LaserPulse, Model-610035).

The time-averaged flow field demonstrated stable statistical convergence when utilizing 600 instantaneous PIV measurements for ensemble averaging. To assure comprehensive statistical reliability, a total of 1000 instantaneous samples were collected and ensemble-averaged, which typically aligns with commonly accepted practices in PIV studies [31–33]. The interval between successive laser pulses (Δt) was selected based on both the local flow velocity and the interrogation window dimensions, ranging from 20 to 80 μ*s*, while images were acquired at a frequency of 15 Hz. Additional details regarding the PIV setup and parameters are summarized in Table 2. The PIV parameters, such as laser sheet thickness, pulsed delay, maximum flow velocity, spatial resolution, etc., are optimized suitably to correctly capture the flow structure and turbulence statistics of the PIV measurement performed, ensuring the correctness and least uncertainty of the results. In order to maintain adequate spatial resolution in the horizontal plane (P^{10}_{x-z}), PIV measurements are acquired in three overlapping 200 mm × 200 mm segments and subsequently merged toobtain a a single flow field. Image processing is performed using a two-pass PIV algorithm within the TSI INSIGHT 4G software. An initial interrogation window size of 64 × 64 pixels is selected, which is subsequently refined to 32 × 32 pixels in

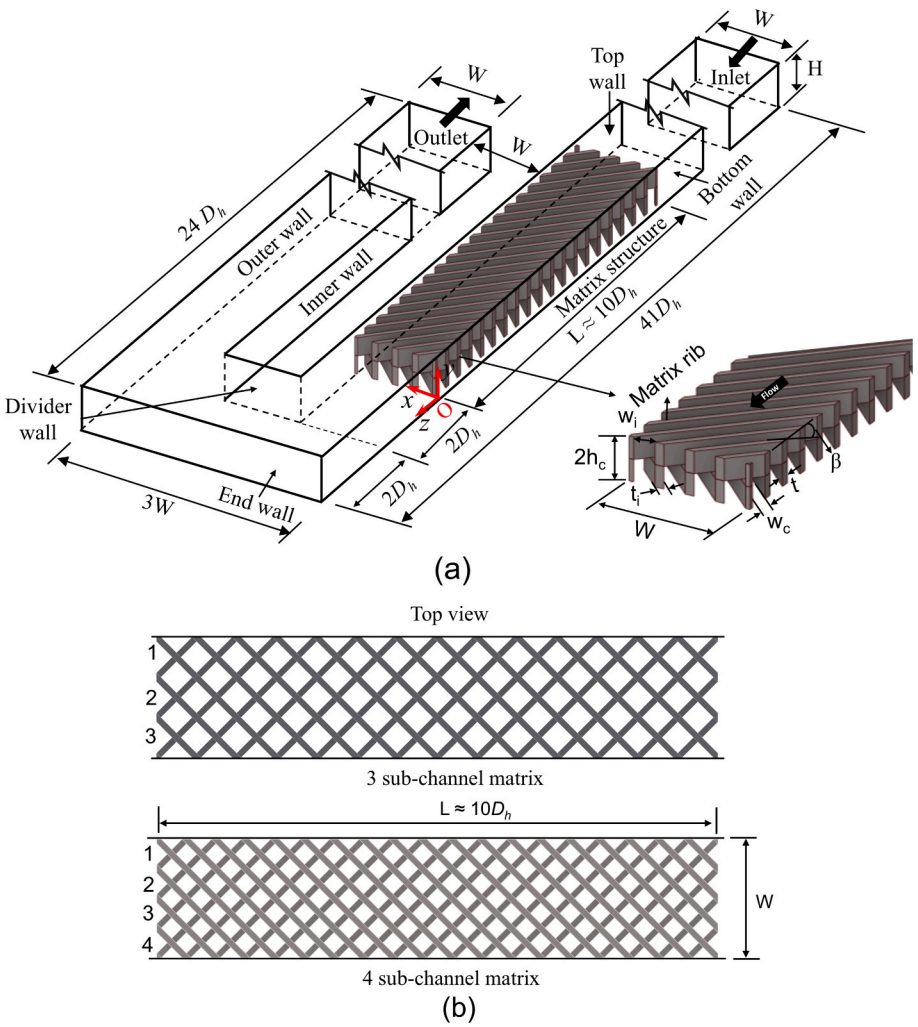

Fig. 3. (a) Schematic of serpentine channel with matrix structure (not on actual scale), (b) top view of 3SC and 4SC matrix structure.

Table 1
Geometric details of matrix structures.

Geometry parameters	W(mm)	H(mm)	L(mm)	h_c(mm)	t(mm)	t_i(mm)	β(mm)	w_c(mm)	w_i(mm)
Matrix with 3 sub-channels	150	46	700	23	7.7	10.9	45°	27.6	39.1
Matrix with 4 sub-channels	150	46	700	23	7.7	10.9	45°	18.8	26.6

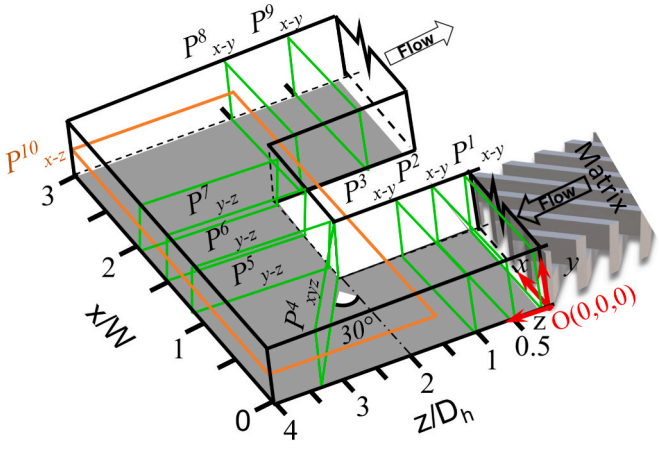

Fig. 4. Illustration of PIV measurement planes with their locations across the bend section.

Table 2
PIV acquisition and processing parameters.

Parameters	cross-stream planes	Streamwise plane
Region of interest	150 × 46 mm^2 – 210 × 46 mm^2	200 × 200 mm^2
Frame rate	15 Hz	15 Hz
Actual image size	2048 × 2048 pixels	2048 × 2048 pixels
Pixel size	7.4 μm × 7.4 μm	7.4 μm × 7.4 μm
Calibration factor	≈ 70 – 80 μm/pixel	≈ 100 μm/pixel
Spatial resolution (*SR*) (window size 32 × 32 pixel)	≈ 2.2 – 2.5 mm	≈ 3.2 mm
Pulse separation, Δt	30 – 80 μs	20 – 40 μs
Interrogation area	(32 × 32) – (64 × 64) $pixel^2$	(32 × 32) – (64 × 64) $pixel^2$

the second pass, depending on local flow condition. This adaptive processing approach enhances spatial resolution in regions exhibiting complex flow patterns while maintaining sufficient dynamic range for accurate measurements. The detailed description of PIV methodology

technique can be found in our earlier publication [4,17,31].

2.2. LCT setup and methodology

Transient liquid crystal thermography (TLCT) has been employed to characterize local heat transfer distributions across the bend section of the matrix-cooled serpentine channel. The experiments used wide-band micro-encapsulated liquid crystal sheets (R40C5W) affixed to the bottom wall of channel, providing full-surface, non-intrusive temperature measurements with high spatial resolution. A heated mainstream approach has been adopted, in which pre-heated air was passed through the channel, producing a step change in the surface temperature. An inline heater positioned upstream of the settling chamber (Fig. 2) regulates the desired inlet air temperature. The local color change response of the LC sheet has been captured using a high-resolution 3-CCD camera system (Toshiba: IK-TF9C) positioned perpendicular to the channel. A uniform illumination has been provided by halogen lamps arranged to minimize reflections and ensure homogeneous light distribution across the test surface. The recorded video (20 fps) has been post-processed using MATLAB to convert RGB images to hue, saturation, and intensity (HSI) values, with the hue component used to map local temperatures. Before experimenting, the TLC sheet was calibrated under in-situ conditions against reference thermocouples to obtain hue-to-temperature correlation [18]. Initially, a 1-D semi-infinite conduction model (**Eq. (1)**) has been used to estimate the local heat transfer coefficient (h) distribution from the transient temperature measurements.

$$\frac{T_w - T_i}{T_a - T_i} = 1 - exp\left(\frac{h^2\alpha_w t}{k_w^2}\right) \times erfc\left(\frac{h\sqrt{\alpha_w t}}{k_w}\right) \tag{1}$$

Here, T_i and T_w are the surface temperature at time $t = 0$ and t, respectively, and T_a is the mainstream air temperature. k_w and α_w are the thermal conductivity and diffusivity of the bottom wall (Perspex), respectively.

The present study primarily focuses on the bend region downstream of the matrix structure, where matrix-induced vortices and strong turning flows are observed, and 1-D conduction model may not predict the actual heat transfer distribution. Therefore, a 3-D conduction-corrected methodology [34] has been utilized based on the 1-D heat transfer results obtained from **Eq. (1)**. A correction factor (suggested by Kingsley-Rowe et al. [35] and Brack et al. [36]) has been applied on obtained 1-D heat transfer results to evaluate 3-D heat transfer, which account for the lateral conduction effect. The 3-D results incorporate both streamwise and spanwise heat diffusion, which provide the actual representation of heat transfer distribution for complex three-dimensional flow phenomena with spatially varying temperature distribution. Also, Sharma and Tariq [34] have reported significant differences between 1D and 3D heat transfer results in regions exhibiting strong three-dimensional flow behavior.

Fig. 5 compares the surface Nusselt number distribution over the bend section of a smooth serpentine channel at $Re = 10000$, evaluated using (a) 1D semi-infinite conduction model and (b) 3D conduction-corrected method. The 3D model [Fig. 5(b)] captures sharper gradients and represents accurate localized heat transfer patterns than the 1D model [Fig. 5(a)], particularly in regions affected by flow separation and mainstream flow (have high velocity gradient). Subsequently, only the 3D conduction-corrected heat transfer (Nusselt number) distribution is presented in the results and discussion. The detailed description of LCT methodology can be found in our previous publications [18,34].

2.3. Data reduction

The vorticity (ω) distribution [33] is calculated as:

$$\omega_x = \frac{\partial w}{\partial y} - \frac{\partial v}{\partial z}\bigg|_{y-z},\ \omega_y = \frac{\partial u}{\partial z} - \frac{\partial w}{\partial x}\bigg|_{z-x},\ and\ \omega_z = \frac{\partial v}{\partial x} - \frac{\partial u}{\partial y}\bigg|_{x-y} \tag{2}$$

Nusselt number is evaluated based on the heat transfer coefficient evaluated using LCT measurement and given as: $Nu = hD_h/k_a$. Here, D_h is the hydraulic diameter of the rectangular channel and k_a is the air thermal conductivity.

Pressure loss is represented in terms of friction factor (f) [37]:

$$f = \frac{\Delta P \times D_h}{2\rho \times V_{avg}^2 \times l} \tag{3}$$

where, (ΔP) is the pressure difference across the bend section (Pa), l is the length of bend section from entry to exit ($z/D_h = 1$), calculated along the channel centreline (m).

The augmentation in heat transfer and friction factor ratio is expressed as Nu/Nu_0, and f/f_0, where Nu_0 and f_0 is the Nusselt number and friction factor evaluated in smooth serpentine channel (without matrix structure). Finally, the thermal performance factor (*TPF*) [37] of matrix-cooled serpentine channel is evaluated as:

$$\text{TPF} = \frac{\overline{Nu}/\overline{Nu_0}}{(f/f_0)^{1/3}} \tag{4}$$

where, $\overline{Nu}/\overline{Nu_0}$ is the overall averaged augmented Nusselt number across bend region.

2.4. Uncertainty analysis

Uncertainty associated with PIV and LCT measurements has been evaluated using the statistical procedure suggested by Kline and McClintock [38]. The major sources of error in instantaneous velocity measurement using PIV ($V = \Delta x/M\Delta t$) are due to magnification factor (M) determined from calibration of the measurement region, seeding

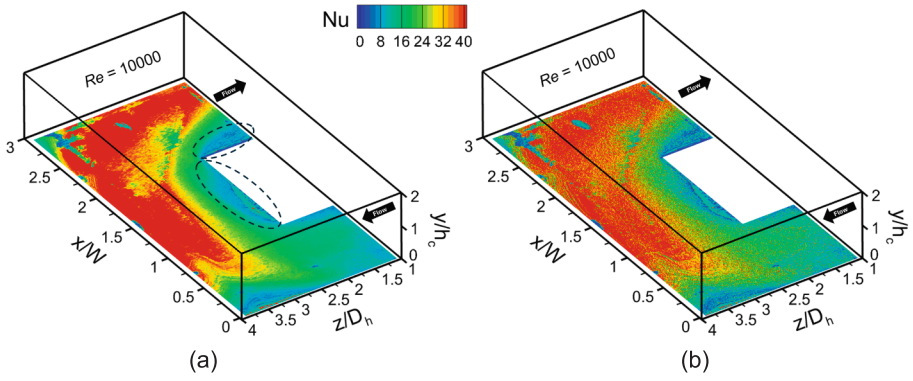

Fig. 5. Nusselt number distribution across the bend region of smooth serpentine channel (without matrix structure) using (a) 1-D solution (y-axis) (b) 3-D solution (y-z-x axis) at $Re = 10000$.

particle displacement (Δx) obtained from the correlation algorithm, and the time interval (Δt) between image pairs. The overall uncertainty for velocity measurement (δ_V) is estimated according to the law of error propagation-

$$\delta_V = \sqrt{\left(\frac{\partial V}{\partial M}\right)^2 {\delta_M}^2 + \left(\frac{\partial V}{\partial(\Delta x)}\right)^2 {\delta_{\Delta x}}^2 + \left(\frac{\partial V}{\partial(\Delta t)}\right)^2 {\delta_{\Delta t}}^2} \quad (5)$$

$$\frac{\delta_V}{V} = \sqrt{\left(\frac{\delta_M}{M}\right)^2 + \left(\frac{\delta_{\Delta x}}{\Delta x}\right)^2 + \left(\frac{\delta_{\Delta t}}{\Delta t}\right)^2} \quad (6)$$

The uncertainty in the magnification factor is mainly caused by errors in the calibration board and optical system. The uncertainty in the particle displacement comprises error in image detection and data processing, which is reduced significantly after post-processing and considered to be ~ 0.1 pixel (commonly accepted value [31,39,40]). The uncertainty in the measurement of the time interval (Δt) is due to uncertainty in pulse timing caused by delay generator and pulse laser. The maximum relative uncertainty associated with magnification factor (M), particle displacement (Δx), and time interval (Δt) is estimated as ~ 8×10^{-3}, 5×10^{-2}, and 7×10^{-5}. As calculated from Eq. (6), the maximum relative uncertainty in instantaneous velocity measurement by PIV system is ~ ± 5.4 % at $Re = 10000$.

The uncertainty in evaluating heat transfer coefficient (h) is mainly due to uncertainty associated with measurement of air temperature (T_a), bottom wall temperature (T_w), initial temperature (T_i), time (t), k_w and α_w. The overall uncertainty for heat transfer coefficient measurement (h) has been estimated as:

$$\frac{\delta_h}{h} = \sqrt{\left(\frac{\delta_{T_a}}{T_a}\right)^2 + \left(\frac{\delta_{T_i}}{T_i}\right)^2 + \left(\frac{\delta_{T_w}}{T_w}\right)^2 + \left(\frac{\delta_t}{t}\right)^2 + \left(\frac{\delta_{k_w}}{k_w}\right)^2 + \left(\frac{\delta_{\alpha_w}}{\alpha_w}\right)^2} \quad (7)$$

The error in temperature measurement (using K-type thermocouple) is ± 0.5 °C, and thus, error in T_a, T_w, and T_i is considered to be ± 0.5 °C. The uncertainty in time (t) is based on the synchronised image acquisition system (frame rate: 20 fps) and has been found to be ± 0.05 s. Additionally, a 3% relative uncertainty has been assumed for k_w and α_w. Hence, the overall relative uncertainty in heat transfer coefficient (h) is ~ ± 5%. Further, the uncertainty associated with Nu and f has been found under ± 5.5% and ± 6.5%, respectively.

3. Results and discussion

Flow evolution and heat transfer behavior across the bend section of matrix-cooled serpentine channel is discussed with 3SC and 4SC matrix structures. Flow characteristics are explained through time-averaged velocity, vorticity, and λ_2 contours along mainstream and cross-streamwise direction. Heat transfer result is explained with Nusselt number distribution and correlated with flow characteristics has been discussed. Heat transfer across the bend section with matrix configuration is compared with that of smooth serpentine channel for reference (augmentation Nusselt number). Finally, thermal–hydraulic performances are evaluated for different parameters under consideration.

3.1. Flow evolution past the matrix structure/before bend

The flow characteristics emanating from the matrix channels (3SC and 4SC) have been explained at a typical $Re = 5000$. Fig. 6 shows the normalized velocity (V_{xy}/w_0) contours at cross-stream plane P^1_{x-y} for 3SC and 4SC matrix. Here, w_0 is the centerline velocity obtained from PIV measurement at $20D_h$ distance from channel inlet and equal to 1.15 m/s, 1.73 m/s and 2.31 m/s for Re = 5000, 7500 and 10000, respectively. In both configurations, the flow exhibits turbulent vortical structures in the form of corotating vortices. The flow emerging from the 3SC and 4SC matrix structures generates three and four distinct anticlockwise rotating vortices, each corresponding to the number of matrix subchannels. The vortices in 3SC configuration are larger, well-separated, and exhibit spatial coherence with moderate interaction. In contrast, the 4SC matrix induces more closely spaced corotating vortices (have narrower subchannels), resulting in stronger vortex–vortex interaction.

The matrix geometry is fabricated and placed in such a way that flow coming out of the upper matrix sub-layer impinges towards inner wall, and lower sub-layer impinges towards outer wall (Fig. 7). Flow near the bottom wall expedites upwards (in transverse direction), and similarly, flows near the upper wall expedite downward, as shown in Fig. 7. Consequently, it creates an anticlockwise swirl in the transverse direction to flow (while viewing from downstream direction of the plane). The presence of vortical flow within the matrix subchannel is not unique to this specific serpentine duct and has been reported by earlier researchers [4,41]. In the present experimental study, flow behavior emanating from the matrix is characterized, confirming the existence of vortices even downstream of the matrix. Therefore, it can be concluded that vortical flow within the matrix duct is a general characteristic of such systems.

Note: we have referred clockwise and anticlockwise directions in vortices throughout the paper when viewing from the end-wall.

The complete flow evolution in the first pass with the 4SC (Fig. 8)

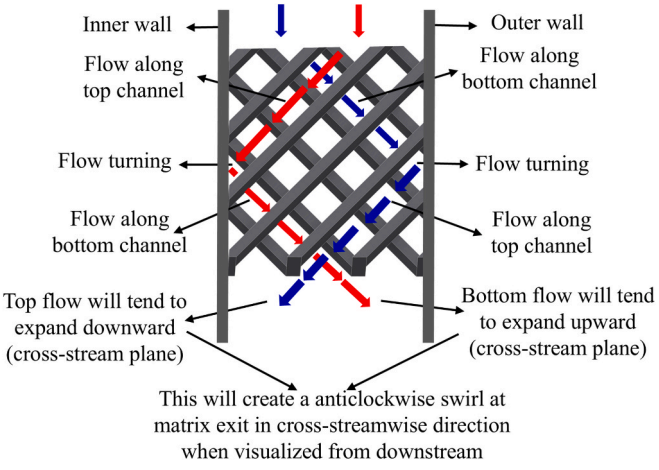

Fig. 7. Illustration of flow evolution by the matrix subchannels.

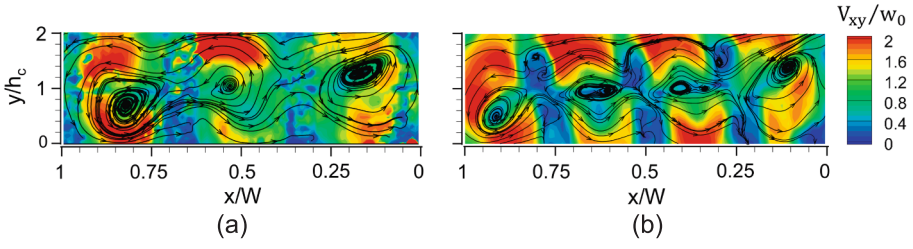

Fig. 6. Velocity contours (V_{xy}/w_0) with streamlines ($Re = 5000$) at plane P^1_{x-y} immediately downstream of the matrix structure for (a) 3SC and (b) 4SC configuration.

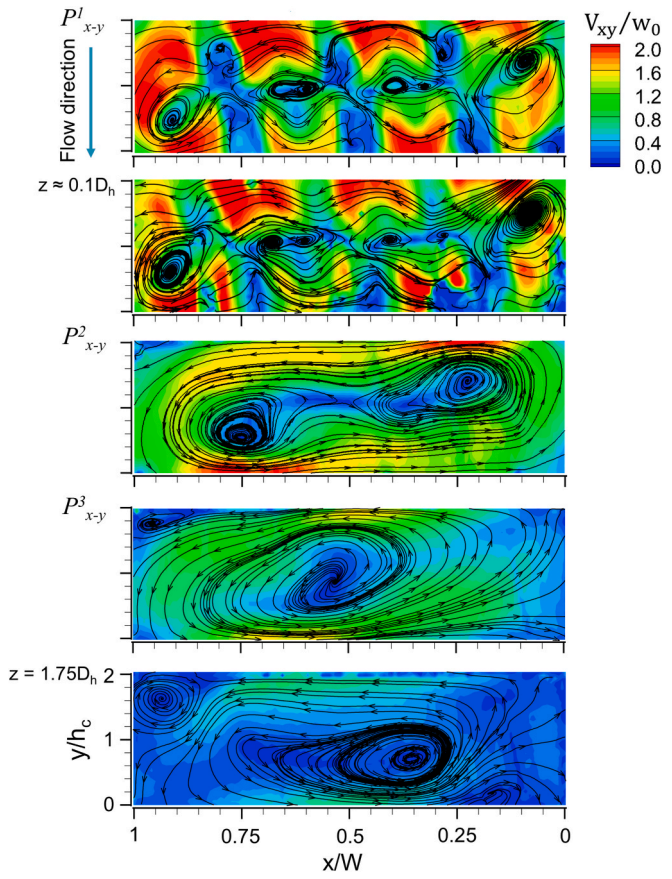

Fig. 8. Velocity contours (V_{xy}/w_0) with streamlines illustrating flow evolution at the planes located along the streamwise direction past the 4SC matrix (Re = 5000).

and 3SC (Fig. 9) matrix configuration is explained using streamlined velocity (V_{xy}/w_0) contours along streamwise direction. Here it is to be highlighted that in Fig. 8, results are presented for five planes situated at various streamwise positions downstream of the matrix exit i.e., $0D_h$ (P^1_{x-y}), $0.15D_h$, $0.5D_h$ (P^2_{x-y}), $1D_h$ (P^3_{x-y}), and $1.75D_h$). The flow

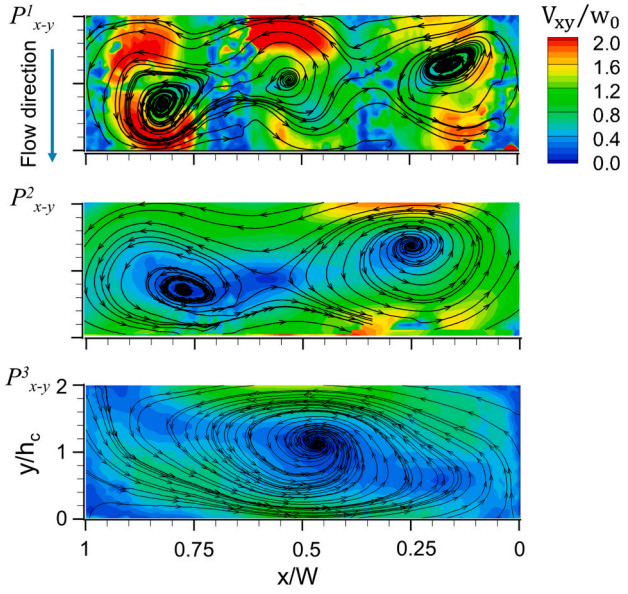

Fig. 9. Velocity contours (V_{xy}/w_0) with streamlines illustrating flow evolution at planes located along streamwise direction past the 3SC matrix (Re = 5000).

characteristics at $0D_h$ and $0.15D_h$ show negligible differences, indicating rapid flow stabilization immediately after the matrix. The plane at $1.75D_h$ is positioned closer to the subsequent bend and will be discussed in detail in the section addressing the flow behavior within the bend region for the 4SC matrix configuration. Consequently, to maintain focus, improve the manuscript's clarity, and conciseness in the discussion for the 3SC case (Fig. 9), results are displayed for only three selected streamwise planes.

As observed in Fig. 8, flow structure near the matrix is symmetric about mid-height ($y/h_c = 1$) and mid-span of the channel ($x/W = 0.5$). The measurement plane P^1_{x-y} is adjacent to matrix structure ($z/D_h \sim 0$), so the flow in front of matrix rib is not developed, and hence low velocity regions are observed between the two vortices. These vortices advance in the first pass, and a completely developed flow structure is observed at $z/D_h \sim 0.14$ distance from P^1_{x-y}. The two pairs of vortices merge into a single pair of vortices at $0.5D_h$ from P^1_{x-y}. As flow advances further, the two vortices coalesce into a single bigger vortex at $z/D_h \sim 1$ from P^1_{x-y}, which spans the entire width of the channel (minor radius = h_c and major radius = W/2). Just before turning near the bend, this bigger vortex structure gets stretched and shifts inwards due to 180° bend.

The small corner vortices at P^3_{x-y} is formed due to the sharp edge of rectangular cross-section channel. It can be observed from Fig. 8 that velocity continuously decreases as flow evolves in the downstream direction, which indicates that flow continuously loses energy from plane P^1_{x-y} to P^3_{x-y}. This might be linked to vortex merging and deterioration of vortex strength during the flow progression [18].

Similar to the observations in 4SC configuration, the three vortices emanating from 3SC matrix (Fig. 9) merge into two vortices and finally coalesce into a single vortex before the at P^3_{x-y}. The velocity magnitude in 3SC-induced vortex structures is lower than that observed in the 4SC matrix, likely due to broader subchannels in 3SC, which results in larger but weaker individual vortices than 4SC matrix. Although the 3SC matrix forms larger, spatially coherent vortical structures, the reduced in-plane velocity (V_{xy}/w_0) results in reduced momentum transfer and cross-stream mixing than 4SC configuration.

The vortex merging phenomenon observed in 4SC configuration (Fig. 8**)** is explained using vorticity ($\omega_z{}^*$) and λ_2-criterion distribution, as shown in Fig. 10. Flow emanating from 4SC matrix has high swirling strength as illustrated by greater values of $\omega_z{}^*$ at plane $P^1_{x\text{-}y}$ within the region of four anticlockwise rotating vortices. The $\omega_z{}^*$ distribution between adjacent vortices illustrates the diffusive state of four co-rotating vortices [42]. In Fig. 10, local smaller vortical zones are seen adjacent to the primary vortices. These regions probably indicate the emergence of weak, secondary vortices that tend to develop in the immediate vicinity of the main vortices at the planes near the immediate exit of the matrix. However, these weaker vortices dissipate as the flow progresses downstream and are no longer visible in the subsequent planes.

As the flow advances downstream ($P^2_{x\text{-}y}$), the four vortices stretch and merge with adjacent vortices to form two vortices. Subsequently, these two vortices also coalesce into a single vortex. The merging of two co-rotating vortices begins when their core size (a) grows sufficiently large relative to their separation distance (b), i.e., $a/b \geq 0.22 - 0.29$ [42,43]. The vortex core radius (a) is calculated from the area enclosed by the vorticity contour line with strength equal to 80 % of the peak value and separation distance (b) is the center-to-center distance between the two co-rotating vortices, as shown in Fig. 10. The core size ratio (a/b) for the vortices at $P^1_{x\text{-}y}$ and $P^2_{x\text{-}y}$ is ≈ 0.25 for both 3SC and 4SC matrix structure, satisfying the condition for the occurrence of the merging process. The merger finally results in a single anticlockwise rotating vortex with average core radius of ≈ 29.5 mm and average $\omega_z{}^*$ ≈ 3 for both matrix structures. This merging phenomenon can also be observed through λ_2-criterion distribution, where high negative λ_2 value shows the vortex core structures at different streamwise positions. Four major vortex cores are observed at plane $P^1_{x\text{-}y}$, which after merging show

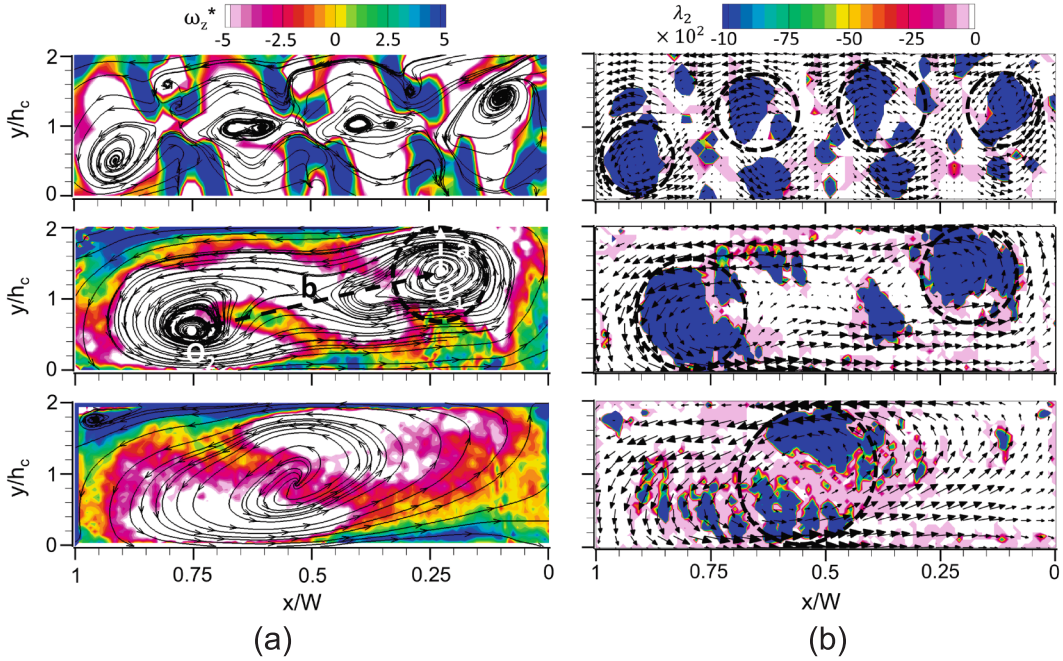

Fig. 10. (a) Vorticity ($\omega_z^* = \omega_z \times D_h/w_0$) and (b) λ_2-criterion distribution ($Re = 5000$) at cross-stream planes past the 4SC matrix illustrating vortex merging phenomena.

two vortex cores at $z/D_h \sim 0.5$ and a single vortex core at $z/D_h \sim 1$.

3.2. Flow evolution in the bend

The flow progression across the bend is explained with the help of velocities contours and streamlines profile at various streamwise and cross-stream planes. Fig. 11 shows the streamlined velocity contour of main flow in the bend section (with 4SC) at horizontal mid-plane (P^{10}_{x-z}). Flow emanating from the matrix channel has higher momentum due to narrow passages of subchannels, and the matrix geometry divides this flow into two streams, as seen at $z/D_h \sim 1.5$ in Fig. 11. One stream moves towards the inner wall, and another one towards the outer wall. This creates a low-velocity magnitude regime observed between two flow streams in the first turn region ($z/D_h \sim 2.2 - 3.2$). Additionally, the sharp curvature of 180° bend deviates the flow toward the inner wall, and a radial pressure gradient towards the inner wall is created in bend section [44]. This causes flow near the outer wall to decelerate and shift inward; however, the higher momentum of flow stream (having high velocity) along the outer wall dominates the radial pressure gradient, and flow strikes the end wall. Thus, creating a negligible corner vortex near the outer corner of bend region ($z/D_h \sim 4$) compared to the large corner recirculation typically observed in a smooth serpentine channel [44]. With increases in Re from 5000 to 10000, overall flow characteristics at the bend inlet remain similar, and only velocity magnitude increases.

As flow turns 90°, centrifugal forces induced by bend curvature push the main flow towards the end wall. Additionally, the sharp edge of divider wall causes flow to separate from the inner wall (here divider wall). Thus, a low-pressure zone is created near the tip of divider wall, and a recirculation zone (or separation zone) is formed which spans the entire divider wall thickness and stretches from $z/D_h = 2$ to $z/D_h \approx 2.35$ for both $Re = 5000$ and 10000. The separated region is characterized by low mean velocity and limited fluid motion. However, at $Re = 10000$, a relatively higher mean velocity is observed near the divider wall [Fig. 11 (b)], likely attributed to intensified vortical activity at higher Re. The higher momentum of flow stream near the inner wall resists continuing to keep the turning flow along the inner wall, which in turn suppresses the growth of recirculation zone compared to recirculation zone size

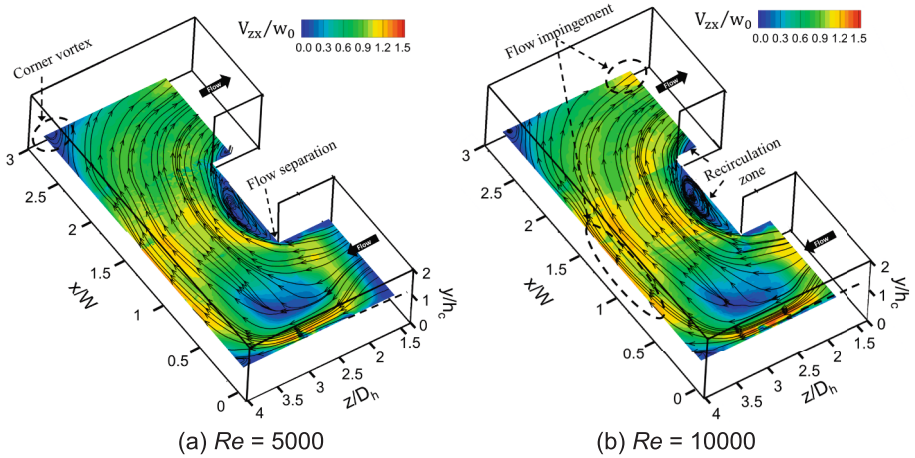

Fig. 11. Velocity contours (V_{zx}/w_0) with streamlines at the horizontal mid plane, P^{10}_{x-z} across bend section with 4SC matrix at $Re = 5000$ and 10000.

observed in smooth serpentine channel [44]. The separated flow stream shifts toward the end-wall and merges with second flow stream to form a mainstream flow region spanning $z/D_h \approx 2.5$ to $z/D_h = 4$. The main flow in bend section is separated into two regions, i.e., mainstream flow region (having high velocity) and recirculation zone (having low velocity), as seen in Fig. 12. These two regions are separated through a small shear layer region ($z/D_h \approx 2.3$ to 2.45) featuring an intense rise in mean velocity and large velocity gradient.

The mean velocity in mainstream flow region is lower than typical observation in smooth serpentine channel [44] due to retarded flow caused by upstream matrix geometry and vortex evolution in cross-streamwise direction before the bend section. With 180° turn, flow again experiences a centrifugal force towards the outer wall and radial pressure gradient towards the inner wall. The lower mainstream velocity in the vicinity of end-wall causes the flow to shift inwards and impinges on the outer wall of bend region, forming a slightly larger corner vortex in second pass of channel [Fig. 11(a)]. Further downstream in second pass the main flow becomes uniform throughout the width of channel. Also, the flow separation due to sharp divider wall further creates a small recirculation zone adjacent to the inner in the second pass. The shifting of mainstream flow toward the end wall and outer wall due to centrifugal force leads to localized flow impingement [see encircled region in Fig. 11(b)]. This impingement enhances turbulence and promotes fluid mixing in adjacent regions. Moreover, the flow stagnation at the end wall contributes to backpressure development, which may reduce the flow velocity within the bend. This impingement effect becomes more pronounced with increases in *Re* from 5000 to 10000.

Flow emanating from the 3SC matrix has lower momentum due to wider subchannels creating weak flow streams with lower mean velocity, as observed at $z/D_h \sim 1.5$ in Fig. 13. Hence, flow stream is unable to attach near the inner wall, and sharp divider wall deflects the flow towards the end wall. This causes formation of a larger recirculation zone ($z/D_h \approx 2$ to $z/D_h \approx 2.5$ and smaller mainstream flow region ($z/D_h \approx 2.8$ to end-wall) compared to observations in bend section with 4SC matrix (Fig. 11). With 180° turn, a larger recirculation zone is formed near the inner wall of second pass, and the mainstream flow region shifts towards the outer wall due to centrifugal force.

Fig. 14 shows the secondary flow evolution at various cross-stream planes in the bend section with 4SC matrix structure at $Re = 5000$. As discussed earlier in Fig. 8, flow before the bend section ($P^1_{x\text{-}y}$) ($z/D_h = 1$) features a swirling flow with a large elliptical anticlockwise rotating vortex at the center. At the bend (30° turn), secondary flow encounters a larger area, which combined with divided flow streams observed in main flow profile (Fig. 11), stretches the center main vortex. Secondary flow divides into two streams with low velocity region in between (P^3_{xyz}),

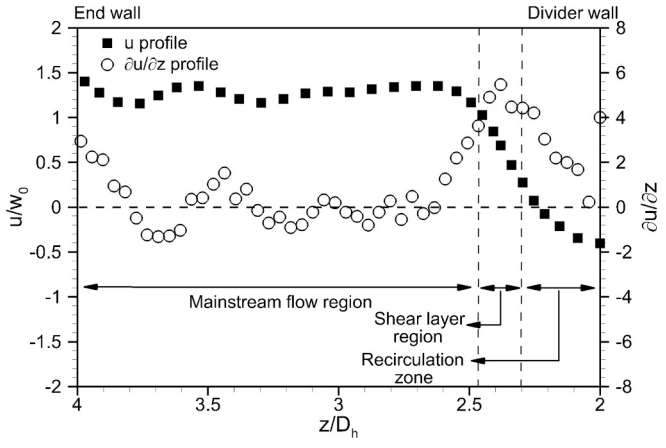

Fig. 12. Normalized velocity component (x-axis) profile (u/w_0) and gradient ($\partial u/\partial z$) distribution along the z-direction at x/W = 1.5 on plane P^{10}_{x-z} with 4SC configuration.

which further confirms the previous observations in main flow profile. With 90° turn, a complex secondary motion is observed featuring side-by-side rotating vortices in mainstream flow region and small vortices in recirculation zone ($P^6_{y\text{-}z}$). The pair of side-by-side counter-rotating vortices observed at plane $P^6_{y\text{-}z}$ in Fig. 14(a) is called Dean vortices, which differs from Dean vortices observed in smooth ducts (with rectangular cross-section) where vortex pair is noted by upper and lower counter-rotating vortices [44]. This change in Dean vortices shape is attributed to vortical flow characteristics before the bend section due to upstream matrix structure compared to undisturbed flow behavior in smooth serpentine channel.

Dean vortices are a distinct class of secondary flow structures that occur specifically in flows through curved channels/pipes due to centrifugal instabilities arising from curvature. In conventional smooth bend, Dean vortices arise from the imbalance between centrifugal forces and the radial pressure gradient (also known as centrifugal instability) [45], leading to two symmetric counter-rotating vortices. However, in the present matrix-cooled serpentine channel, the rib-matrix elements disturb this balance, causing asymmetry and distortion in the vortex structure. The interaction between curvature-induced secondary flow and matrix-induced perturbations modifies the strength and stability of the vortices, making them notably different from those in conventional smooth bends.

Fig. 14(b) illustrates the comprehensive visualization for this complex secondary flow development at bend center ($P^5_{y\text{-}z} - P^7_{y\text{-}z}$). The stretched clockwise rotating vortex at P^3_{xyz} [Fig. 14(a)] breaks and forms a pair of counter-rotating vortices at x/W = 1.15 ($P^5_{y\text{-}z}$). This imparts a circular motion to the fluid particles near outer wall, resulting in the evolution of another vortex. The centrifugal instability causes this evolving secondary flow motion to form a pair of major side-by-side counter-rotating vortices in mainstream flow region and few smaller vortices in recirculation zone at $P^6_{y\text{-}z}$. These secondary flow structures (in mainstream flow region) have high in-plane velocity (V_{yz}/w_0) which enhance transverse fluid mixing. In contrast, small weak vortices near divider wall indicate limited fluid motion (flow entrapment) due to flow separation. Just before 180° turn (at x/W = 1.85, $P^7_{y\text{-}z}$), bend curvature causes the flow to turn, which forces center main vortices to get stretched towards inner wall and increases the in-plane velocity (V_{yz}/w_0). The vortex near outer wall shifts outwards and upwards under the combined action of centrifugal force and upward thrust generated by the impingement effect of anticlockwise rotating vortex on the bottom wall.

With 180° turn [Fig. 14(a)], the centrifugal force shifts the secondary flow structure outwards. The clockwise rotating vortices come close and interact with anticlockwise rotating vortices while dissipating extra energy imparted from main flow while turning. Their interaction results in the formation of a single vortex structure at the top corner of outer wall (at $P^8_{x\text{-}y}$). With further advancement, the secondary flow structure further dissipates its energy, resulting in a continuous reduction of in-plane velocity (V_{xy}/w_0).

Effect of *Re* (= 5000, 10000) on secondary flow characteristics in the bend section is discussed at 90° plane ($P^6_{y\text{-}z}$). Fig. 15 shows the streamlines velocity (V_{yz}/w_0), vorticity (ω^*_x) and λ_2—criterion contours superimposed with velocity vector at $P^5_{y\text{-}z}$ with $Re = 5000$ and 10000. With increases in *Re* from 5000 to 10000, the in-plane velocity (V_{yz}/w_0) and vorticity magnitude (ω^*_x) decrease, although the overall flow structure and vortex pattern remain qualitatively similar. The reduction in V_{yz}/w_0 and ω^*_x is attributed to the increase in mainstream velocity component (V_{zx}/w_0) in bend section at $Re = 10000$ [see Fig. 11(b)], resulting in weaker secondary flow strength (Fig. 15). Additionally, the λ_2 criterion distribution also illustrates the weaker vortex core strength at $Re = 1000$ compared to $Re = 5000$. Among the counter-rotating vortex pair, the clockwise-rotating vortex exhibits a stronger core, represented by a high

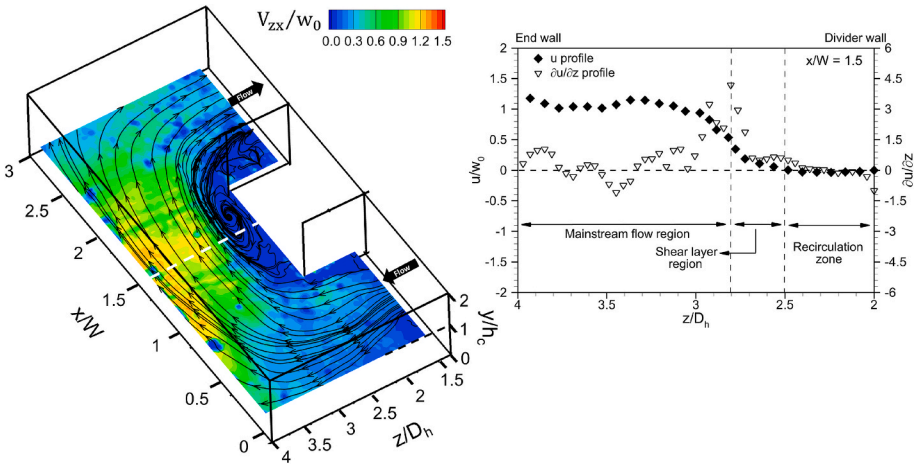

Fig. 13. Velocity contours (V_{zx}/w_0) with streamlines at the horizontal mid-plane, P^{10}_{x-z} and velocity component (x-axis) profile (u/w_0) and gradient ($\partial u/\partial z$) distribution along the z-axis at x/W = 1.5 with 3SC matrix at Re = 5000.

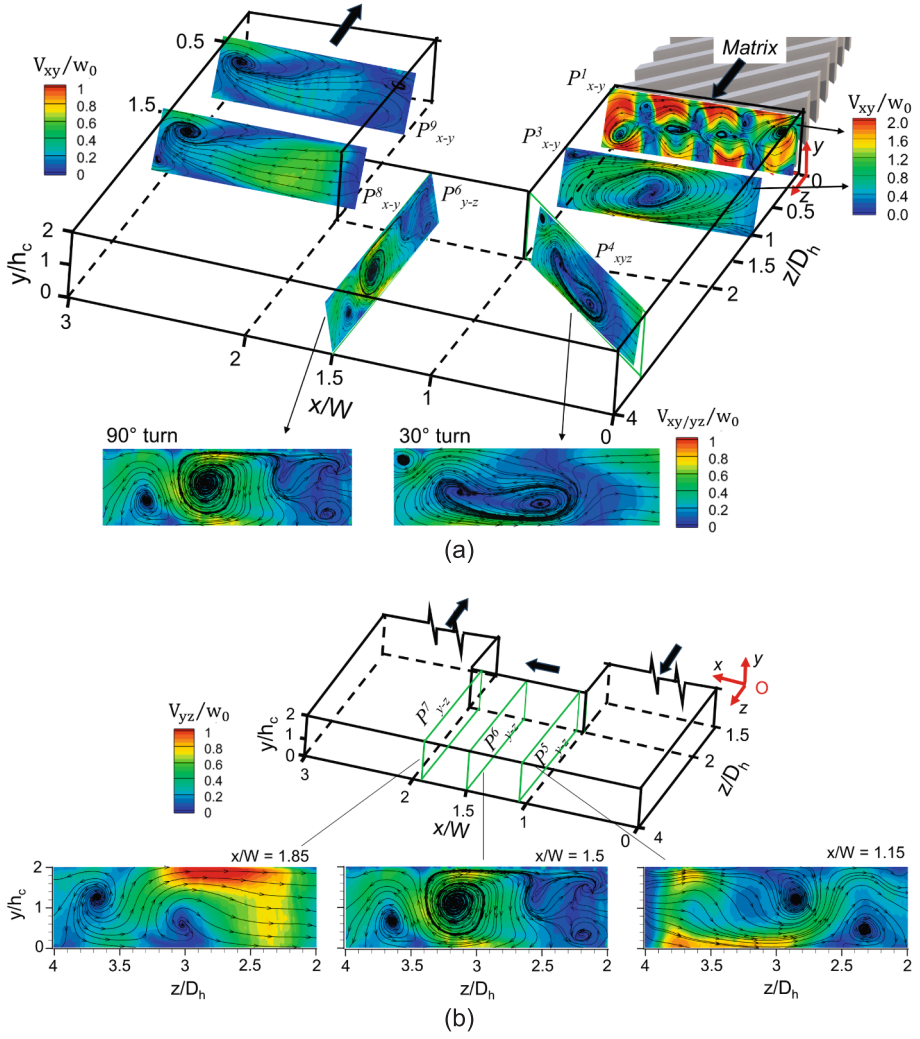

Fig. 14. (a) Velocity contours (V_{xy}/w_0 *and* V_{yz}/w_0) with streamlines at various cross-streamwise planes and (b) secondary flow development between planes P^5_{y-z} and P^7_{y-z} in the bend section with 4SC matrix (Re = 5000).

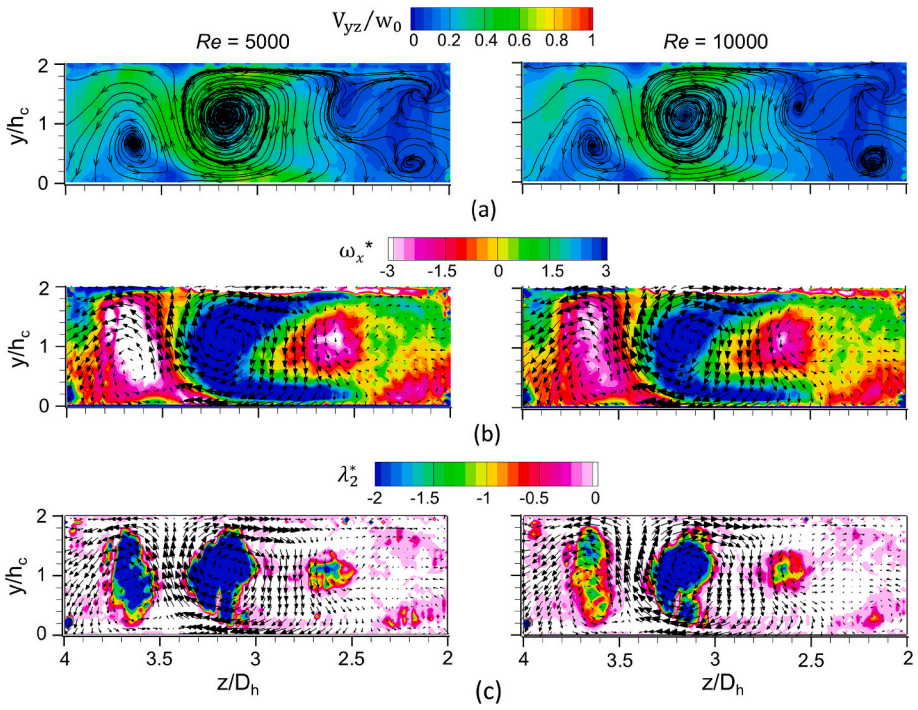

Fig. 15. (a) Velocity (V_{yz}/w_0) contour with streamlines, (b) Vorticity ($\omega_x^* = \omega_x \times D_h/w_0$) and (c) λ_2—criterion contours superimposed with velocity vector at plane P^6_{y-z} with Re = 5000 and 10,000 in 4SC configuration.

negative λ_2 value. These observations suggest that while the overall secondary flow profile remains unchanged with increasing Reynolds number, its strength diminishes due to the increase in mainstream flow component in the bend section.

3.3. Heat transfer characteristics

Surface heat transfer distribution across the bend section with 3SC and 4SC matrix configuration has been discussed at Re = 5000–10000. It is important to note that Nu contours for intermediate Re = 7500 are not presented in the discussion to avoid redundancy while maintaining clarity, as the heat transfer characteristics were found to be nearly identical to those observed at Re = 5000 and 10000. However, Re = 7500 has been included in the thermal–hydraulic performance evaluation in Section 3.6 to ensure a complete performance comparison across the studied range.

Fig. 16 shows the Nusselt number (Nu) contour with 3SC and 4SC matrix structure at a typical Re = 5000. A strong correlation between heat transfer distribution and main flow behavior is observed. The footprints of three and four localized Nu zones are observed downstream of each 3SC matrix and 4SC matrix, respectively, which is consistent with flow observations in Fig. 6. Nu values downstream of the matrix are higher due to the higher momentum of flow emanating from the matrix subchannels and sharply decreases along streamwise direction due to

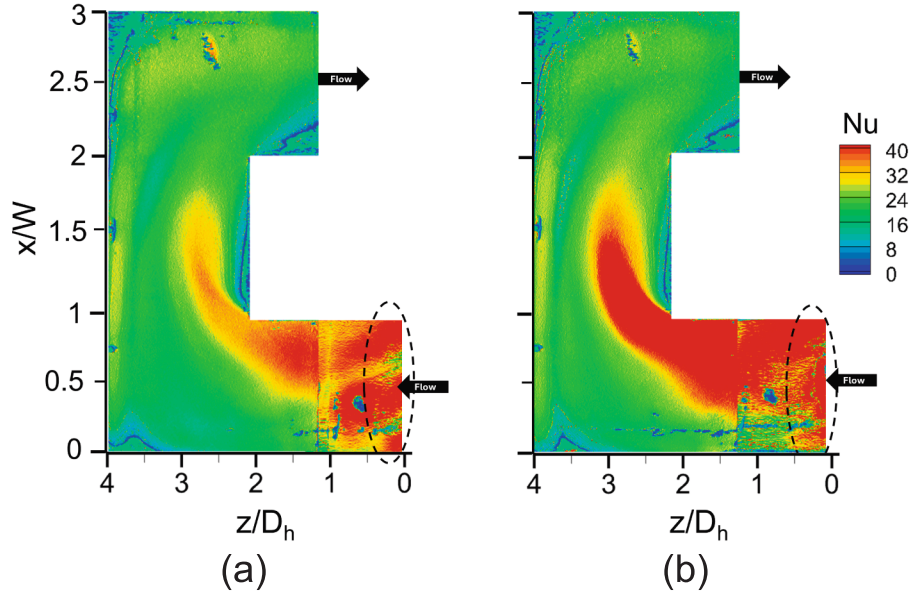

Fig. 16. Nusselt number contours downstream of matrix with (a) 3SC and (b) 4SC configuration at a typical Re = 5000.

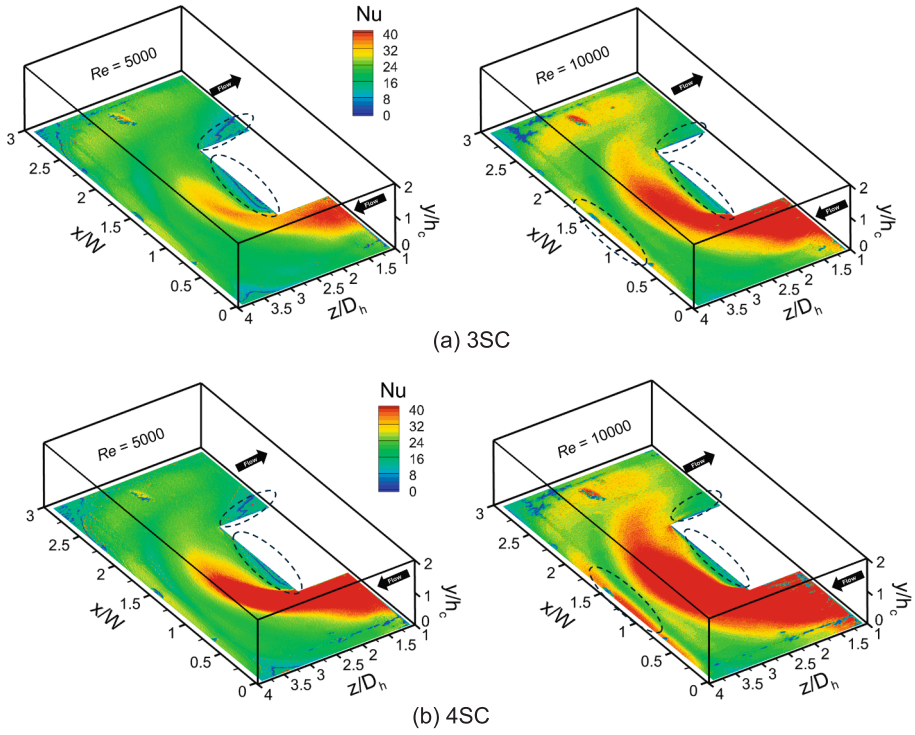

Fig. 17. Nusselt number contours across the bend section with (a) 3SC and (b) 4SC matrix at $Re = 5000$ and 10000.

decrease in flow strength (Fig. 8). Overall, 4SC matrix shows higher *Nu* values than 3SC matrix due to higher flow strength.

Fig. 17 shows the *Nu* contours across the bend section with 3SC and 4SC configurations at $Re = 5000$ and 10000. Just before the bend (Fig. 17), *Nu* distribution is stretched across the spanwise direction and shifts inwards as observed earlier from main and secondary flow observation. Upon 90° turn, the heat transfer distribution follows the main flow profile with higher *Nu* value in the regime of bulk flow stream due to higher flow momentum (see Fig. 11). The bend region near the divider wall shows lower heat transfer values than mainstream flow region. In general, heat transfer is higher in bend section with 4SC matrix than 3SC matrix structure. Additionally, heat transfer increases

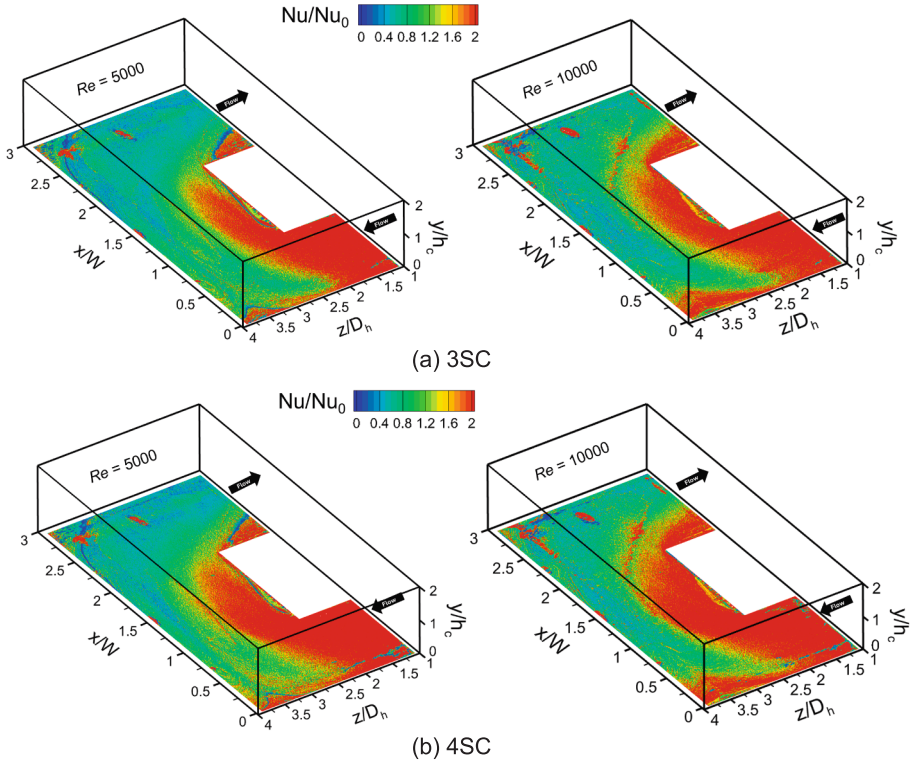

Fig. 18. Normalized Nusselt number (Nu/Nu_0) contours across the bend section with (a) 3SC and (b) 4SC matrix configuration at $Re = 5000$ and 10000.

with increasing *Re* from 5000 to 10000. Lower heat transfer value is observed in recirculation zone, which can create a hot spot zone due to flow entrapment. A smaller footprint of hot spot zone is observed with 4SC matrix compared to 3SC matrix, likely due to smaller size of recirculation zone. This low *Nu* zone is also observed downstream near the inner wall of second pass. However, with increase in *Re*, the hotpot zone size decreases and vanishes completely at $Re = 10000$. This is likely attributed to increased vortical motion near divider wall at $Re = 10000$ as observed in Fig. 11(b). A high *Nu* region is observed towards the end wall due to flow impingement.

Fig. 18 shows the augmentation Nusselt number (Nu/Nu_0) distribution with 3SC and 4SC matrix at $Re = 5000$ and 10000. A strong heat transfer augmentation occurs upstream of bend section and near the divider wall, which is more pronounced with 4SC matrix than 3SC matrix. However, a poor heat transfer augmentation (i.e., $Nu/Nu_0 \leq 1$) is observed towards the outer side of the bend section. The enhancement observed upstream of bend is attributed to the direct impingement of matrix-induced vortical structures on the bottom wall. The larger size of recirculation zone near divider wall causes larger hot spot zone (with low Nu_0 values) in smooth serpentine channel (see Fig. 5), which cause Nu/Nu_0 values to increase sharply near divider wall. Conversely, mainstream flow region with higher Nu_0 is towards end-wall in smooth serpentine channel, which reduces the Nu/Nu_0 values. The heat transfer distribution at $z/D_h = 2$ is divided into two zones as observed in streamlined velocity contours of main flow profile (Fig. 11). The above observations in Nusselt number distribution indicate that heat transfer directly correlates with the main flow profile.

The quantitative analysis of augmentation in heat transfer with matrix structure is discussed. Fig. 19 shows the spanwise-averaged Nusselt number ($\overline{Nu}/\overline{Nu_0}$) distribution along various streamwise locations across the bend section. The highest enhancement in heat transfer is observed immediately downstream of matrix structure (before bend/0° turn), with 4SC matrix producing maximum augmentation with $\overline{Nu}/\overline{Nu_0} \sim 5.82$ at $Re = 5000$ and ~ 8.46 at $Re = 10000$. This corresponds to 482 % and 746 % increases in heat transfer compared to the smooth channel (without matrix), respectively. The 3SC configuration shows a lower augmentation ($\overline{Nu}/\overline{Nu_0}$) ~ 5.63 at $Re = 10000$, reflecting a 463 % enhancement in heat transfer compared to the smooth channel (without matrix).

As the flow progresses downstream, $\overline{Nu}/\overline{Nu_0}$ decreases at 30° and 90°, although moderate enhancement persists due to Dean vortices formation and improved fluid mixing. At 30° turn, $\overline{Nu}/\overline{Nu_0}$ values for 3SC and 4SC configuration are ~ 1.61 and ~ 2.45 respectively for $Re = 10000$. At 90° turn, a secondary rise in heat transfer is observed, particularly for 4SC at $Re = 10000$, i.e., $\overline{Nu}/\overline{Nu_0} \sim 3.24$, while $\overline{Nu}/\overline{Nu_0} \sim 1.88$ 3SC matrix shows 1.88 (88 % gain). The 4SC configuration maintains a higher $\overline{Nu}/\overline{Nu_0}$ throughout, indicating stronger main flow and secondary flow development. A sharp decline in $\overline{Nu}/\overline{Nu_0} \sim 0.57$—0.98 is observed near the 150° location across all configurations

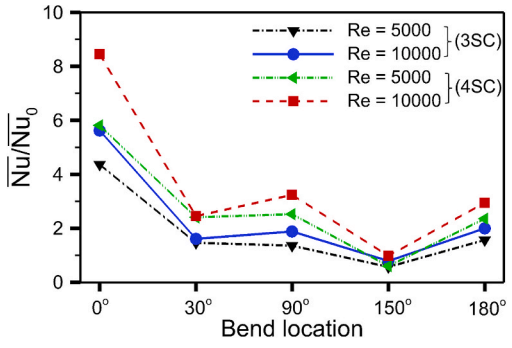

Fig. 19. Spanwise-averaged augmentation ($\overline{Nu}/\overline{Nu_0}$) distribution along various locations along bend section.

and *Re*, suggesting weak flow strength and diminished turbulence in this region. However, at the 180° turn (bend exit), heat transfer again improves. At $Re = 10000$), $\overline{Nu}/\overline{Nu_0}$ with 4SC and 3SC matrix is ≈ 2.94 and 2, respectively, representing a 194 % and 100 % increase over smooth duct conditions. The low heat transfer zone near inner wall of second pass in smooth serpentine channel likely contributes to increased Nu/Nu_0 values (see Fig. 5).

Overall, the 4SC matrix configuration consistently outperforms the 3SC matrix structure across all *Re*, with greater differences observed at $Re = 10000$. These findings confirm that matrix cooling, particularly with 4SC matrix (higher subchannel density), significantly augments heat transfer across the bend, especially in high Reynolds number flows where vortex strength and mixing are more pronounced.

3.4. Effect of secondary flows on heat transfer

Surface heat transfer results in section 3.3 show a strong correlation between secondary flows and local Nusselt number characteristics. The localized Nusselt number (*Nu*) distribution and normalized vorticity (ω_x^*) contours with streamlines across the plane $P^1_{x\text{-}y}$ with 3SC and 4SC matrix configurations ($Re = 5000$) are presented in Fig. 20. For both cases, the number of *Nu* peaks match the number of vortices generated, confirming the close correlation between vortex impingement and localized surface heat transfer enhancement. The surface impingements break the boundary layer, thus increasing momentum and energy transfer. The 3SC configuration shows three major peaks, with maximum *Nu* values reaching ~ 55–60, while the 4SC configuration exhibits four pronounced peaks, with local *Nu* reaching ~ 90–95, indicating stronger convective enhancement. *Nu* distribution also reveals that the magnitude and sharpness of peaks are greater in 4SC case, suggesting that more concentrated and stronger vortices improve local wall cooling effectiveness. The valleys in *Nu* profile indicate regions of relatively weak flow reattachment or reduced wall shear.

Fig. 21 presents the localized Nusselt number distribution and normalized vorticity (ω^*) contours superimposed with velocity vector at plane $P^3_{x\text{-}y}$ (0° turn), $P^6_{y\text{-}z}$ (90° turn) and $P^8_{x\text{-}y}$ (180° turn) with 3SC and 4SC matrix configurations ($Re = 5000$). Upstream of the bend ($P^3_{x\text{-}y}$), *Nu* increases in regions where the vortex impinges on the bottom wall and decreases where the vortex lifts away from the surface [Fig. 21(a)]. In 3SC configuration, heat transfer peaks around x/W ≈ 0.55–0.65, with *Nu* reaching ≈ 40. For 4SC configuration, a higher *Nu* ≈ 60 is observed near x/W ≈ 0.7, consistent with the stronger vortex impingement. Additionally, the inward shift of the vortex toward x/W = 1 as the flow turns into the bend reduces wall shear and convective transport near the outer side (x/W < 0.5), resulting in lower *Nu* values.

At the 90° turn ($P^6_{y\text{-}z}$), single bigger vortices evolve into a complex secondary flow pattern [Fig. 21(b)]. A progressive reduction in vortex strength is observed during this evolution, as indicated by the decline in vorticity (ω*) from the upstream plane ($P^3_{x\text{-}y}$) to the bend center ($P^6_{y\text{-}z}$). Both configurations exhibit Dean-type counter-rotating secondary flows induced by curvature, which enhance mixing and generate distinct local zones of high and low heat transfer over the plane. In 3SC configuration, primary recirculation region near the divider wall ($z/D_h \approx 2.0$–2.3) exhibits low *Nu* values due to flow entrapment. *Nu* increases sharply between $z/D_h \approx 2.4$–3, peaking at *Nu*≈ 32, due to vortex impingement on the bottom wall. Beyond this, *Nu* gradually decreases as the vortex lifts away from the surface, and a gradual decline is seen up to $z/D_h \approx 3.5$, where *Nu* becomes minimum (≈ 20) under the combined effect of counter-rotating vortices leaving the bottom surface. Similarly, the local *Nu* increases and decreases towards the end-wall in anticlockwise rotating vortex regime, as seen in Fig. 21(b).

In the 4SC configuration, Dean vortices occupy a wider span with a smaller recirculation zone compared to 3SC. The 4SC configuration exhibits a higher peak *Nu* ≈ 42 at $z/D_h \approx 2.9$, attributed to the higher

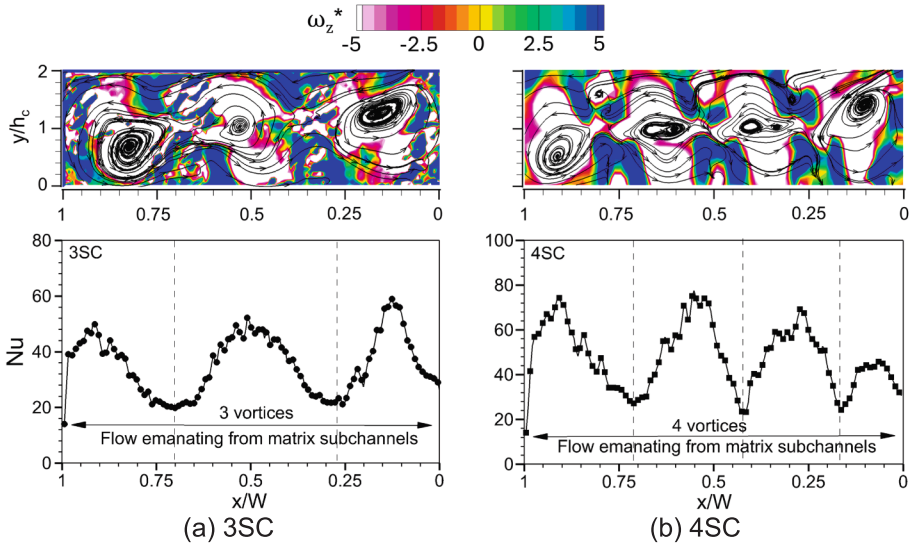

Fig. 20. Vorticity contours ($\omega_x^* = \omega_x \times D_h/w_0$) with streamlines and local Nusselt number distribution ($Re = 5000$) on plane P^1_{x-y} for (a) 3SC and (b) 4SC configurations.

vorticity strength compared to 3SC. Similar to observation in 3SC, *Nu* gradually decreases up to $z/D_h \approx 3.6$, where *Nu* becomes minimum (≈ 18). The ratio of *Nu* between vortex impingement and lift-off zones is ~ 2 times in 4SC and ~ 1.5 in 3SC configuration, indicating greater thermal enhancement by vortex dynamics in the 4SC configuration.

At 180° turn (P^8_{x-y}), the vortex strength further decreases, as observed by decreasing values of ω^* from entry to exit of the bend [Fig. 21(c)]. Both 3SC and 4SC configurations exhibit similar flow structures, characterized by a single dominant vortex whose core shifts outward toward the outer wall due to centrifugal forces. This similarity suggests that most of the energetic secondary motion induced by matrix structures has dissipated by the bend center, resulting in a weaker vortex field. However, the 3SC configuration shows slightly stronger vorticity strength, influenced by its main flow profile. As shown in Fig. 13, mainstream flow in 3SC shifts toward the outer wall in second pass, which enhances curvature-induced secondary motion at 180° turn, resulting in locally higher vorticity despite prior decay. Hence, the increased vorticity at P^8_{x-y} is attributed to geometry-driven flow evolution, not sustained vortex strength. In both configurations, the vortex core is centered near $x/W \approx 2.75$–3, with comparable vorticity strength. *Nu* distribution shows a gradual increase from the inner wall ($x/W = 2.0$) to the vortex region ($x/W \approx 2.75$). Near the inner wall, a relatively lower *Nu* value of the order ~ 10 in the 3SC case and ~ 8 in 4SC is observed due to flow detachment and reduced near-wall momentum. *Nu* rises steadily, peaking at ~ 25 near $x/W \approx 2.75$, in the vicinity of vortex core. The 3SC configuration exhibits marginally higher *Nu* toward outer wall, consistent with secondary flow characteristics.

The observations in flow behavior in streamwise and cross-streamwise directions manifest the heat transfer distribution in the bend region. The local Nusselt number distribution follows secondary flow observations, illustrating the strong footprint of flow condition on heat transfer. Although primary/main flow has a dominating effect on the heat transfer distribution, the secondary flow structures and their interaction feature significant changes in localized *Nu* values.

3.5. Effect on turbulence

Turbulence kinetic energy distribution provides insight into the energy dissipation along secondary flow evolution with matrix structure. Fig. 22 presents the normalized turbulent kinetic energy ($\overline{TKE}$) averaged across various cross-stream planes across bend region with 3SC and 4SC matrix configurations. In the 3SC configuration, a high level of $\overline{TKE}$ (≈ 0.15) is observed at P^1_{x-y}, where flow (3 vortices) emanates from matrix structure (turbulence promoter). With flow progression to $z/D_h \approx 0.5$ (P^2_{x-y}), three vortices merge into two vortices and a sharp peak in turbulence ($\overline{TKE} \approx 0.2$) is observed. It is likely attributed to the complete spatial development of vortical structures at $0.5D_h$ distance away from the matrix subchannels. However, as the flow evolves downstream, turbulence diffusion with vortex merging of two vortices into a single vortex reduces $\overline{TKE}$, leading to a ≈ 33% drop in $\overline{TKE}$ at P^3_{x-y}. Similar turbulence decay during vortex merging has also been reported by Hopfinger & van Heist [46]. As flow advances through the bend, a continuous decay in turbulence (≈ 65% reduction) is observed in 3SC configuration from P^3_{x-y} to P^6_{y-z} (center of bend), and ~ 30% drop between P^6_{y-z} and P^8_{y-z} (bend exit), reflecting energy dissipation as vortical strength weakens.

The 4SC configuration shows a similar trend, with a slightly lower TKE (≈ 0.13) observed in secondary flow (4 vortices) emanating from matrix (P^1_{x-y}), which increases to a peak TKE (≈ 0.14) at P^2_{x-y}. Subsequently, TKE decays steadily throughout the bend from entry (P^3_{x-y}) to exit P^8_{y-z}. These reductions reflect the continuous weakening of vortical structures during turning, consistent with previous observations in vorticity distribution (Fig. 21). Overall, TKE decreases by 79% and 89% in 3SC and 4SC configurations, indicating higher flow resistance (pressure penalty) in 4SC configuration. Notably, unlike in the smooth serpentine channel where turbulence increases across the bend [17], matrix configurations show a continuous decay in turbulence, highlighting that the presence of the matrix structure, rather than bend curvature alone, governs the turbulence behavior.

3.6. Thermal-hydraulic performance

The overall effect of matrix structure on thermal–hydraulic performance across the bend section has been discussed. Surface averaged augmentation Nusselt number ($\overline{Nu_A}/\overline{Nu_0}$) and normalized friction factor (f/f_0) are evaluated across the bend section. Table 3 summarizes the thermal hydraulic performance with various matrix configurations (3SCand 4SC) and Reynolds numbers ($Re = 5000$, 7500 and 10000). The results show that both matrix configurations significantly enhance heat transfer in the bend section relative to the smooth channel. Additionally, the Nusselt number augmentation and friction factor increase with the

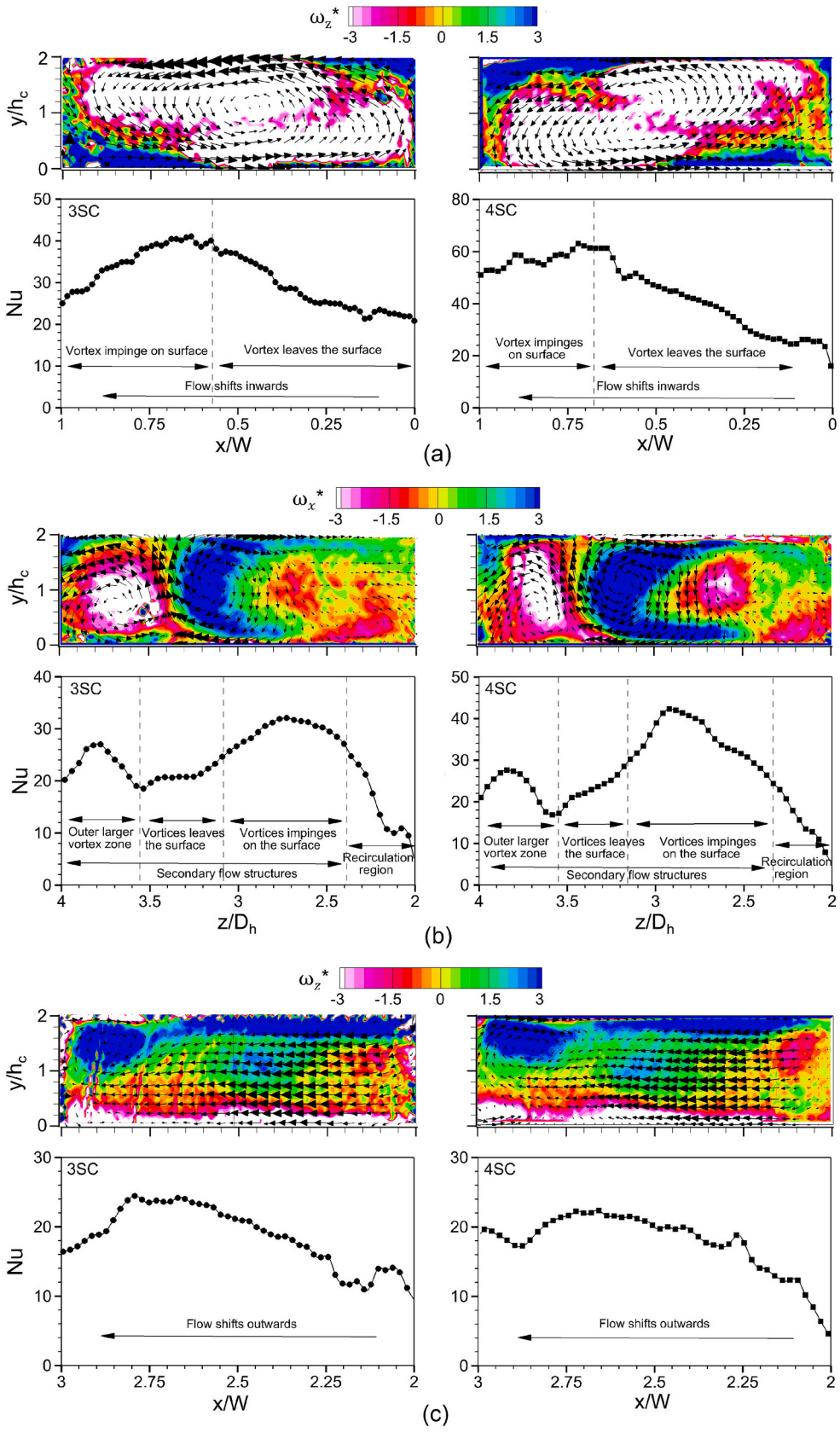

Fig. 21. Normalized vorticity pattern ($\omega^* = \omega \times D_h/w_0$) and local Nusselt number distribution ($Re = 5000$) at plane (a) $P^3_{x\text{-}y}$ (0° turn), (b) $P^6_{y\text{-}z}$ (90° turn) and (c) $P^8_{x\text{-}y}$ (180° turn) with 3SC (left) and 4SC (right) configurations.

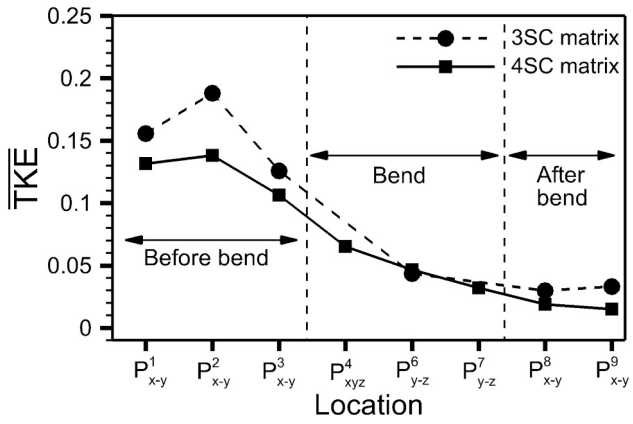

Fig. 22. Variation of spanwise averaged turbulent kinetic energy ($\overline{TKE} = TKE/w_0^2$) across the bend section ($Re = 5000$) with 3SC and 4SC matrix.

Table 3
Thermal-hydraulic performance parameters of bend section for 3SC and 4SC matrix.

	$\overline{Nu_A}/\overline{Nu_0}$		f/f_0		TPF	
Re	3SC	4SC	3SC	4SC	3SC	4SC
5000	1.80	1.85	0.93	0.95	1.84	1.88
7500	1.96	2.12	0.96	1.06	1.99	2.08
10,000	2.05	2.33	0.95	0.98	2.09	2.34

number of subchannels, indicating stronger secondary flow development. At $Re = 5000$, the 3SC and 4SC configuration increases heat transfer by ~ 80% and ~ 85% relative to the smooth channel, leading to thermal performance factor (TPF) of 1.84 and 1.88, respectively.

At $Re = 10000$, $\overline{Nu_A}/\overline{Nu_0}$ improves by ~ 105% and ~ 133% with 3SC and 4SC configuration, respectively. Despite this, the friction penalty remains nearly constant with increasing Reynolds number and remains close to that of the smooth channel. As a result, TPF improves reaching ≈ 2.09 for 3SC and ≈ 2.34 for 4SC, which shows that the 4SC matrix delivers better thermal performance with moderate hydraulic loss than 3SC.

A direct correlation is observed between the frictional penalty and the drop in turbulent kinetic energy (TKE) across the bend section. From matrix outlet ($P^1_{x\text{-}y}$) to bend exit ($P^8_{x\text{-}y}$), the 3SC configuration shows a 79% reduction in TKE, while the 4SC configuration exhibits a higher decay of 89%. This greater loss of turbulence energy in the 4SC configuration corresponds to increased flow resistance, as confirmed by the higher friction factor ($f/f_0 = 0.98$) compared to 3SC ($f/f_0 = 0.95$) at $Re = 10000$.

Overall, the 4SC matrix provides higher heat transfer enhancement and thermal performance factor (TPF) than the 3SC configuration across all Reynolds numbers. The improvement is more pronounced at higher flow rates, where increased subchannels promote stronger vortex-induced mixing and better convective heat transport. These results demonstrate that matrix-cooled designs, particularly with 4SC configuration, are significantly effective for internal cooling systems operating at high Reynolds numbers, such as in gas turbines, fuel cells, and compact heat exchangers, where efficient heat transfer with limited pressure drop is essential.

4. Conclusion

Flow evolution and heat transfer characteristics downstream of the matrix are evaluated using PIV and LCT techniques for two matrix configurations (3SC and 4SC) and three Reynolds number ($Re = 5000$, 7500 and 10000). A comprehensive insight into critical flow features, including mainstream flow, secondary flow, recirculation zone, and Dean-type vortices, has been presented. Heat transfer characteristics are presented in the form of Nu and $\overline{Nu}/\overline{Nu_0}$ distribution and correlated with flow characteristics. The major findings of the present experimental effort are summarized as follows:

1. Matrix structures generate strong co-rotating vortices, which coalesce into a single vortex before the onset of bend. This vortical flow produces complex secondary flows, including Dean-type vortices in the bend region.
2. The surface heat transfer distribution significantly follows the primary flow dynamics in the bend region. An intense enhancement in localized heat transfer is observed due to the impinging jet-like effect of vortices, while a steep decrement in heat transfer is observed due to vortices leaving the surface. Overall, matrix cooling provides higher heat transfer in the bend regime than a smooth channel ($\overline{Nu_A}/\overline{Nu_0} \geq 1$).
3. 4SC matrix configuration exhibits stronger vortex-induced mixing, resulting in higher local and area-averaged heat transfer performance compared to 3SC. At $Re = 10000$, augmentation Nusselt number ($\overline{Nu_A}/\overline{Nu_0}$) reaches ~ 105% and ~ 133% in 3SC and 4SC configuration, respectively.
4. Despite enhanced vortex activity, the friction penalty remains low. At $Re = 10000$, normalized friction factors for 3SC and 4SC configurations are of the order (f/f_0) = 0.95 and 0.98, respectively.
5. Thermal performance factor (TPF) improves with increasing Reynolds number, reaching 2.34 for 4SC and 2.09 for 3SC at $Re = 10000$, demonstrating the superior thermal–hydraulic performance of 4SC design.
6. A direct correlation is observed between TKE decay and frictional loss, where 4SC exhibits a higher TKE drop (~89 %) from inlet to bend exit, compared to 3SC (~ 79%), indicating stronger energy dissipation and corresponding pressure drop.

CRediT authorship contribution statement

Arun Chand: Writing – review & editing, Writing – original draft, Visualization, Methodology, Investigation, Data curation, Conceptualization. **Nishab Ali:** Writing – review & editing, Visualization, Methodology, Conceptualization. **Andallib Tariq:** Writing – review & editing, Supervision, Resources, Funding acquisition, Data curation, Conceptualization.

Declaration of competing interest

The authors declare that they have no known competing financial interests or personal relationships that could have appeared to influence the work reported in this paper.

Acknowledgment

The authors are grateful to the Indian Institute of Technology Roorkee (IITR) and duly acknowledge the financial support of the Gas Turbine Research Establishment (GTRE), India, in funding the research facility at AVTAR lab (vide Grant Code DRD-759-MID) at mechanical and industrial engineering department, IITR.

Data availability

The data that support the findings of this study are available from the corresponding author upon reasonable request.

References

[1] J.C. Han, S. Dutta, S. Ekkad, Gas turbine heat transfer and cooling technology, CRC Press (2012), https://doi.org/10.1201/b13616.

[2] C. Carcasci, B. Facchini, M. Pievaroli, L. Tarchi, A. Ceccherini, L. Innocenti, Heat transfer and pressure loss measurements of matrix cooling geometries for gas turbine airfoils, J. Turbomach. 136 (2014) 1–8, https://doi.org/10.1115/1.4028237.
[3] A. Tariq, A.N. Prajapati, Heat transfer characteristics within the matrix cooling channels, J. Turbomach. 143 (2021) 1–13, https://doi.org/10.1115/1.4050113.
[4] N. Ali, A. Tariq, Experimental study of flow physics and heat transfer across the matrix subchannels, Appl. Therm. Eng. 273 (2025) 126541, https://doi.org/10.1016/j.applthermaleng.2025.126541.
[5] V. Gorelov, M. Goikhenberg, V. Malkov, The investigation of heat transfer in cooled blades of gas turbines, in: 26th Jt. Propuls. Conf., American Institute of Aeronautics and Astronautics, Reston, Virigina, 1990: p. 2144. Doi: 10.2514/6.1990-2144.
[6] R.S. Bunker, Latticework (Vortex) Cooling Effectiveness: Part 1 — Stationary Channel Experiments, in: Vol. 3 Turbo Expo 2004, ASMEDC, 2004: pp. 909–918. Doi: 10.1115/GT2004-54157.
[7] K. Saha, S. Acharya, C. Nakamata, Heat transfer enhancement and thermal performance of lattice structures for internal cooling of airfoil trailing edges, J. Therm. Sci. Eng. Appl. 5 (2013) 1–9, https://doi.org/10.1115/1.4007277.
[8] H. Deng, K. Wang, J. Zhu, W. Pan, Experimental study on heat transfer and flow resistance in improved latticework cooling channels, J. Therm. Sci. 22 (2013) 250–256, https://doi.org/10.1007/s11630-013-0620-3.
[9] S. Bu, Z. Yang, W. Zhang, H. Liu, H. Sun, Research on the thermal performance of matrix cooling channel with response surface methodology, Appl. Therm. Eng. 109 (2016) 75–86, https://doi.org/10.1016/j.applthermaleng.2016.08.005.
[10] A.N. Prajapati, A. Tariq, A comparative study of heat transfer characteristics and pressure drop in matrix structures, in: Vol. 1 Compressors, Fans, Pumps; Turbines; Heat Transf. Struct. Dyn., American Society of Mechanical Engineers, 2019: pp. 1–10. Doi: 10.1115/GTINDIA2019-2550.
[11] L. Li, H. Deng, H. Li, Y. Huang, Systematical numerical investigations on heat transfer performance of latticework channel, Int. Commun. Heat Mass Transf. 138 (2022) 106367, https://doi.org/10.1016/j.icheatmasstransfer.2022.106367.
[12] Q. Ruan, L. Xu, L. Xi, D. Ren, J. Gao, Y. Li, Optimization design and experimental research on cooling performance of U-shaped latticework cooling structure with perforations used for gas turbine blade, Appl. Therm. Eng. 247 (2024) 123044, https://doi.org/10.1016/j.applthermaleng.2024.123044.
[13] J. Li, B. Yu, X. Li, S. Bu, A. Wang, Multi-jet impingement cooling in the leading edge of turbine blade using matrix as internal structure, Appl. Therm. Eng. 250 (2024) 123531, https://doi.org/10.1016/j.applthermaleng.2024.123531.
[14] Y. Xiao, H. Deng, H. Jiang, L. Li, K. Yan, Y. Huang, Flow and heat transfer characteristics of adaptive latticework structure: the effect of wall boundaries, Appl. Therm. Eng. 274 (2025) 126549, https://doi.org/10.1016/j.applthermaleng.2025.126549.
[15] B. Wang, H. Deng, L. Li, H. Li, Design and test of smart heat exchanger based on shape memory alloys, Appl. Therm. Eng. 221 (2023) 119911, https://doi.org/10.1016/j.applthermaleng.2022.119911.
[16] L. Li, H. Deng, H. Li, Y. Xiao, Y. Huang, Flow and heat transfer characteristics in adaptive latticework structure designed using shape memory alloys, Appl. Therm. Eng. 240 (2024) 122217, https://doi.org/10.1016/j.applthermaleng.2023.122217.
[17] N. Ali, A. Tariq, Laminar and turbulent flow development study in a rectangular duct with 180° sharp bend by using stereo particle image velocimetry and liquid crystal thermography measurements, Phys. Fluids 35 (2023), https://doi.org/10.1063/5.0131308.
[18] N. Ali, A. Tariq, Aerothermal characteristics past a matrix structure inside a rectangular serpentine passage, Appl. Therm. Eng. 237 (2024), https://doi.org/10.1016/j.applthermaleng.2023.121796.
[19] A. Pothérat, L. Zhang, Dean flow and vortex shedding in a three-dimensional 180° sharp bend, (2018). http://arxiv.org/abs/1807.10950.
[20] H. Wang, M.J. Ni, N.M. Zhang, Three-dimensional magnetohydrodynamic flow around a 180° sharp bend under transverse magnetic field, Phys. Fluids 34 (2022), https://doi.org/10.1063/5.0079163.
[21] Y.M. Chung, P.G. Tucker, D.G. Roychowdhury, Unsteady laminar flow and convective heat transfer in a sharp 180° bend, n.d. www.elsevier.com/locate/ijhff.
[22] K. Arul Prakash, Steady and unsteady numerical investigations of laminar fluid flow and heat transfer in a 180◦ bend with bypass, Int. J. Heat Mass Transf. 151 (2020). Doi: 10.1016/j.ijheatmasstransfer.2020.119357.
[23] H. Kahraman, M.F. Orhan, Flow field bipolar plates in a proton exchange membrane fuel cell: analysis & modeling, Energy Convers. Manag. 133 (2017) 363–384, https://doi.org/10.1016/j.enconman.2016.10.053.
[24] S.Y. Son, K.D. Kihm, J.C. Han, PIV flow measurements for heat transfer characterization in two-pass square channels with smooth and 90° ribbed walls, Int. J. Heat Mass Transf. 45 (2002) 4809–4822, https://doi.org/10.1016/S0017-9310(02)00192-8.
[25] R. Liu, H. Li, R. You, Z. Tao, Experimental investigation of turbulent flow in a two-pass channel with different U-shaped bends, AIP Adv. 10 (2020), https://doi.org/10.1063/5.0011444.
[26] N. Ali, A. Tariq, Saifullah, Vortex evolution and merging mechanism across 180° sharp bend for laminar inflow, Phys. Fluids 35 (2023), https://doi.org/10.1063/5.0157739.
[27] D.E. Metzger, C.W. Plevich, C.S. Fan, Pressure loss through sharp 180 deg turns in smooth rectangular channels, J. Eng. Gas Turbines Power 106 (1984) 677–681, https://doi.org/10.1115/1.3239623.
[28] Y. Shimizu, K. Sugino, Hydraulic losses and flow patterns of a swirling flow in U-bends, Bull. JSME 23 (1980) 1443–1450, https://doi.org/10.1299/jsme1958.23.1443.
[29] O. Kitoh, Swirling flow through a bend, J. Fluid Mech. 175 (1987) 429–446, https://doi.org/10.1017/S0022112087000466.
[30] M. Anwer, R.M.C. So, Swirling turbulent flow through a curved pipe: Part I: effect of swirl and bend curvature, Exp. Fluids Exp. Methods Their Appl. to Fluid Flow 14 (1993) 85–96, https://doi.org/10.1007/BF00196992.
[31] M.S. Ali, A. Tariq, B.K. Gandhi, Flow and heat transfer investigation behind trapezoidal rib using PIV and LCT measurements, Exp. Fluids 54 (2013), https://doi.org/10.1007/s00348-013-1520-8.
[32] L. Wang, M. Salewski, B. Sundén, Turbulent flow in a ribbed channel: flow structures in the vicinity of a rib, Exp. Therm Fluid Sci. 34 (2010) 165–176, https://doi.org/10.1016/j.expthermflusci.2009.10.005.
[33] N. Sharma, A. Tariq, M. Mishra, Experimental investigation of flow structure due to truncated prismatic rib turbulators using particle image velocimetry, Exp. Therm Fluid Sci. 91 (2018) 479–508, https://doi.org/10.1016/j.expthermflusci.2017.11.004.
[34] V. Sharma, A. Tariq, Lateral conduction effect study using 2-D transient liquid crystal measurement, Therm. Sci. Eng. Prog. 60 (2025) 103456, https://doi.org/10.1016/j.tsep.2025.103456.
[35] J.R. Kingsley-Rowe, G.D. Lock, J.M. Owen, Transient heat transfer measurements using thermochromic liquid crystal: lateral-conduction error, Int. J. Heat Fluid Flow 26 (2005) 256–263, https://doi.org/10.1016/j.ijheatfluidflow.2004.08.011.
[36] S. Brack, R. Poser, J. Von Wolfersdorf, An approach to consider lateral heat conduction effects in the evaluation process of transient heat transfer measurements using TLC, Int. J. Therm. Sci. 107 (2016) 289–302, https://doi.org/10.1016/j.ijthermalsci.2016.03.028.
[37] N. Kaewchoothong, P. Narato, C. Nuntadusit, Experimental investigation of the heat transfer characteristics and thermal performance inside a ribbed serpentine channel during rotational effects, Exp. Therm Fluid Sci. 111 (2020) 109973, https://doi.org/10.1016/j.expthermflusci.2019.109973.
[38] S.J. Kline, F.A. McClintock, Kline_McClintock1953.pdf, Mech. Eng. (1953) 3–8.
[39] L. Wang, J. Hejcik, B. Sunden, PIV measurement of separated flow in a square channel with streamwise periodic ribs on one wall, J. Fluids Eng. Trans. ASME 129 (2007) 834–841, https://doi.org/10.1115/1.2742723.
[40] H. Li, J. Shi, R. You, Z. Tao, Particle image velocimetry measurements of turbulent flows in rotating square ribbed ducts, Phys. Fluids 34 (2022), https://doi.org/10.1063/5.0097193.
[41] S.R. Ramireddy, S.P. Gurusiddappa, V. Kesavan, S.K. Kumar, Computational study of flow and heat transfer in matrix cooling channels, ASME 2014 Gas Turb. India Conf. GTINDIA 2014 (2014) 1–7, https://doi.org/10.1115/GTINDIA2014-8252.
[42] C. Cerretelli, C.H.K. Williamson, The physical mechanism for vortex merging, J. Fluid Mech. 475 (2003) 41–77, https://doi.org/10.1017/S0022112002002847.
[43] C. Josserand, M. Rossi, The merging of two co-rotating vortices: a numerical study, Eur. J. Mech. B/fluids 26 (2007) 779–794, https://doi.org/10.1016/j.euromechflu.2007.02.005.
[44] A. Chand, A. Tariq, Aerothermal characterization of divider wall geometry inside serpentine channel, Int. J. Therm. Sci. 212 (2025) 109760, https://doi.org/10.1016/j.ijthermalsci.2025.109760.
[45] P.G. Drazin, Centrifugal Instability, in: Hydrodyn. Stab., Second, Cambridge University Press, 2004: pp. 69–123. Doi: 10.1017/CBO9780511616938.005.
[46] E.J. Hopfinger, J.F. Van Heist, Vortices in Rotating Fluids (1993) 241–289, https://doi.org/10.1146/annurev.fluid.25.1.241.